

Advances in Synthesis and Defect Properties of Halide Perovskite Nanocrystals: Experimental and Theoretical Perspectives



Bhawna, Supriti Ghorui, Aftab Alam, and M. Aslam

Abstract Metal halide perovskites are gaining attention for their interesting opto-electronic properties which result in their promising use for commercial applications. The ease in the fabrication and processability of perovskite nanocrystals with high photoluminescence quantum yield has tremendously attracted the research community and since then various approaches for their synthesis have been developed. This chapter focuses on various size and shape-controlled solution-based synthesis methods for perovskite nanocrystals. Furthermore, synthesis of defect-free perovskite nanocrystals to attain long-term stability along with high efficiency is the primary focus of the growing research community. Therefore, deeper insight into defect properties in perovskite nanocrystals is crucial despite of their defect-tolerant nature. Thus, the purpose of this chapter is twofold (i) to give a complete understanding of various facile synthesis strategies for metal halide perovskite nanocrystals while discussing their advantages and limitations and (ii) to facilitate an in-depth insight about the formation of native defects both from the experimental and theoretical perspectives.

Keywords Hybrid perovskites · Photovoltaic · Synthesis Strategies · Defects · DFT simulation

1 Introduction

Metal halide perovskites (MHPs) have been known since a long time and the first work was reported by H. L. Wells in 1893 [1]. However, it was only the 1990s when they got traction from the scientific community due to their promising electronic and optical properties [2, 3]. The term perovskite was coined after the famous Russian

Bhawna · S. Ghorui · A. Alam · M. Aslam (✉)
Department of Physics, Indian Institute of Technology Bombay, Mumbai, India
e-mail: m.aslam@iitb.ac.in

A. Alam
e-mail: aftab@iitb.ac.in

mineralogist Lev Perovski and belongs to the class of materials which have a general formula ABX_3 . Here, in halide perovskites, A can be an inorganic cation like cesium (Cs) or organic cation like methylammonium (MA), formamidinium (FA) or their mixture, B typically refers to lead (Pb) or tin (Sn) and X is a halide anion namely chloride (Cl^-), bromide (Br^-) or iodide (I^-). Based on the kind of A cation, the halide-based perovskites can be classified in hybrid (A belongs to organic group) and all-inorganic (A is an inorganic cation) perovskites. Initially, lead halide perovskites (LHPs) were used as visible-light sensitizers in dye-sensitized solar cells in 2009 [4]. It took another 3 years to realize the impressive charge transport properties of these MHPs, in addition to the strong bandgap absorption, to achieve modest power-conversion efficiency (PCE) of 3–7% [5, 6]. Since then, a surge in research output in LHPs has been seen which resulted in a certified PCE of over 25% for single-junction perovskite-based solar cells in a very short duration [7]. The reason behind such a high PCE is high absorption coefficient ($>1 \times 10^4 \text{ cm}^{-1}$), low Urbach energies, long charge carrier diffusion lengths ($>100 \text{ nm}$), high carrier mobility and long carrier lifetime [8, 9].

Surprisingly, LHPs not only provide a strong ground for the photovoltaic application but also pose as attractive candidates for the light emitting diodes (LEDs) due to strong direct band-to-band transitions, relatively low non-radiative recombination rates and high color purity [10–13]. However, the low photoluminescence quantum yield (PLQY) associated with the bulk perovskites limit their use in LEDs. This is mainly because of the small exciton binding energies (resulting in low radiative recombination) and the existence of mobile ionic defects (characterised by low formation energies) in the bulk perovskite structures. Halide perovskite films are easily grown from their precursor solution via facile solution processable method at low temperatures, but, the defects in the bulk as well as at the grain boundaries or interfaces are created and act as centres for fast non-radiative decays [14, 15]. This motivated the researchers to move to perovskite nanocrystals (NCs) in search for better PLQYs. Interestingly, optical and electronic properties of MHPs are size-dependent and can be tuned by changing the size of the crystals to the nano-regime. Further, one can play with the dimensionality (from 3D to *quasi*-2D to 2D, also known as layered perovskites) of MHPs by using long-chain alkylammonium cations as separators of the octahedron slabs. The number of the octahedral layers ($m = 1$ to ∞) provides flexibility in tuning emission wavelength and the exciton binding energies in layered perovskites [16–18]. The MHP NCs facilitate efficient light emission with near-unity PLQY as opposed to the low PLQYs seen in bulk perovskites making them a potential candidate for LEDs [19].

The research on MHP NCs took off after the first report on colloidal halide perovskite $MAPbBr_3$ with a PLQY of $\sim 20\%$ by Schmidt et al. in 2014 [20]. The selection and use of appropriate capping ligands in the preparation routine enable not only the control on the size of these crystals in the nanometer range but also help in passivating the surface defects. Gonzalez-Carrero et al. further improved the synthesis of highly luminescent $MAPbBr_3$ with an impressive PLQY of $\sim 80\%$, however, the particles obtained were highly irregular in shape [21]. In early 2015, the hot-injection (HI) method was introduced by Protesescu and group in order to

gain narrow particle size distribution of colloidal LHP NCs. This method resulted in the synthesis of monodisperse CsPbX_3 ($X = \text{halide or their mixed halides}$) NCs. Later, the room-temperature synthesis of colloidal MAPbX_3 NCs were proposed by Zhang et al. using ligand-assisted reprecipitation (LARP) method which resulted in the efficient emission (PLQY $\sim 70\%$) with the added benefit of color-tunability [22]. Since then, several attempts have been made to regulate the shape and size of MHP NCs by changing reaction temperature, capping ligands etc. This resulted in attaining different morphologies ranging from nanowires (NWs) to nanosheets (NSs) to nanoplatelets (NPLs) to quantum dots (QDs) [23–27]. Extensive research on improving the synthesis methods of LHP NCs have been done in order to produce highly monodisperse with near-unity emission and high colloidal stability [28, 29]. Further, the composition and size of these NCs can be tuned using post-synthetic transformations such as through exfoliation or ion migration [30, 31]. However, due to the presence of surface defects/trap states and the loss of ligand binding to the NCs during the purification and isolation procedures, the PLQYs of MHPs get affected strongly [17, 32]. In this regard, the post-synthetic treatment with functional molecules/metal halides helps in improving their PLQYs [33, 34]. On one hand, ease in synthesis of MHPs has led the researchers to utilize these active materials for applications such as lasers, solar cells, LEDs, photodetectors etc., whereas, on the other hand, they possess substantial health hazards due to the presence of lead and also suffer from instability issues which includes degradation at interfaces [35, 36] and inter-diffusion of ions from different materials [37]. To address these concerns and to preserve the crystal structure of perovskite, replacement of Pb^{2+} with heterovalent substitution of a monovalent, B (Ag^+ , Au^+ , Cu^+ , Na^+) and a trivalent cation, B' (Bi^{3+} , Au^{3+} , In^{3+} , Sb^{3+}) to form a quaternary double perovskite (elapsolite), $\text{A}_2\text{B}(\text{I})\text{B}'(\text{III})\text{X}_6$ (where $\text{A} = \text{Cs}$, and $\text{X} = \text{Cl, Br, I}$) have been proposed recently [38–46]. However, these newly developed structures are facing various other problems such as indirect bandgap and low PLQYs.

In MHPs, the presence of different kinds of chemical interactions results in their characteristic “soft” structure, which exposes the structure to a large number of defects. Synthesis of defect-free MHP NCs with a single radiative (excitonic) recombination pathway to achieve a near-unity PLQY is the main focus of the growing research community. Various studies show the creation of favourable halogen vacancy due to their low formation energies as opposed to Cs/Pb vacancies, antisites or interstitial sites in these NCs [47]. Moreover, the large surface area in addition to the increased number of the dangling bonds in case of NCs result in the increment in the density of trap states than in single-crystals or polycrystalline thin films [48]. In this light, it becomes imperative to understand the role of defects in the photophysics of MHPs [49, 50].

2 Introducing MHP NCs: Crystal Structure and Defect-Tolerance

Since the first observation of optical-related quantum effects in the nm-sized semiconductors in early 1980s [51, 52], tremendous attention has been drawn towards developing strategies to synthesize high-quality MHP NCs for their further utilisation in practical applications [53–55]. The fabrication of MHP NCs not only helps in achieving high PLQY (~90%) but also helps in attaining enhanced emission which is tunable across the whole visible range and in screening the surface traps [56]. The captivating results shifted the attention of research community to work on these interesting class of semiconducting materials.

3D perovskites belong to the class with general formula $A^+B^{2+}X_3$, where, A is a monovalent cation (metal or organic cation; Cs^+ , MA^+ , FA^+ or mixed cation), B is a divalent cation (Pb^{2+} , Sn^{2+} etc.) and X is a halide anion (Cl^- , Br^- and I^-). The structure comprises of the corner-sharing BX_6 octahedra which repeat in all the directions to give 3D framework whereas, A lies in the cuboctahedral cavities (coordinating with 12 X anions) formed by this continuous network and puts a limit on the size of the enclosed cation [57]. To assess the structural stability and the size of A^+ cation that can effectively fit in the 3D perovskite structure, the Goldschmidt tolerance factor, $t = (R_A + R_X)/\sqrt{2}(R_B + R_X)$ and the octahedral factor, $\mu = R_B/R_X$ are utilised (Fig. 1). Here, ionic radii of A, B and X ions are represented by R_A , R_B and R_X . The perovskite structure is stable when $0.8 < t < 1$ and $0.442 < \mu < 0.895$ [58, 59]. The perovskite structures such as $CsPbI_3$ and $FAPbI_3$ have tolerance factor of ~0.8 and ~1 (at the edge of the limit), respectively and therefore, readily undergo transition to stable phases i.e., orthorhombic and tetragonal phases even at room temperature (RT), popularly known as “yellow phases” (Fig. 1) [60, 61].

The prime reason behind the easy fabrication of highly crystalline MHP thin films even at room temperature is the presence of ionic bonding in the perovskite structure [62]. Another significant feature regarding the success of MHPs in the opto-electronic applications is their defect-tolerance which helps a semiconductor to regain its properties despite the presence of a large number of crystallographic defects (see Fig. 2). Various factors for instance, preparation of precursor solution, heat treatment, crystallization etc. strongly influence the defect formation during perovskite film fabrication [63]. Density functional theory (DFT) calculations suggest the introduction of shallow trap states due to the formation of point defects such as halogen vacancies with low formation energies. In semiconductors, due to the antibonding and bonding character of conduction band (CB) and valence band (VB), respectively, deep defect states are generally formed after removal of an atom [64]. On the other hand, MHPs have CB and VB both with antibonding character, where, the CB edge is formed from the interaction between Pb-s and X-p orbitals and VB edge from the interaction between Pb-p and X-p orbitals. Mainly, the defects states are present near or within the VB edge due to very strong antibonding coupling between Pb-s and X-p orbitals, which results in raising the VB edge. Whereas, ionic character is shown by the CB edge due to the weak coupling between Pb-p and X-p orbitals

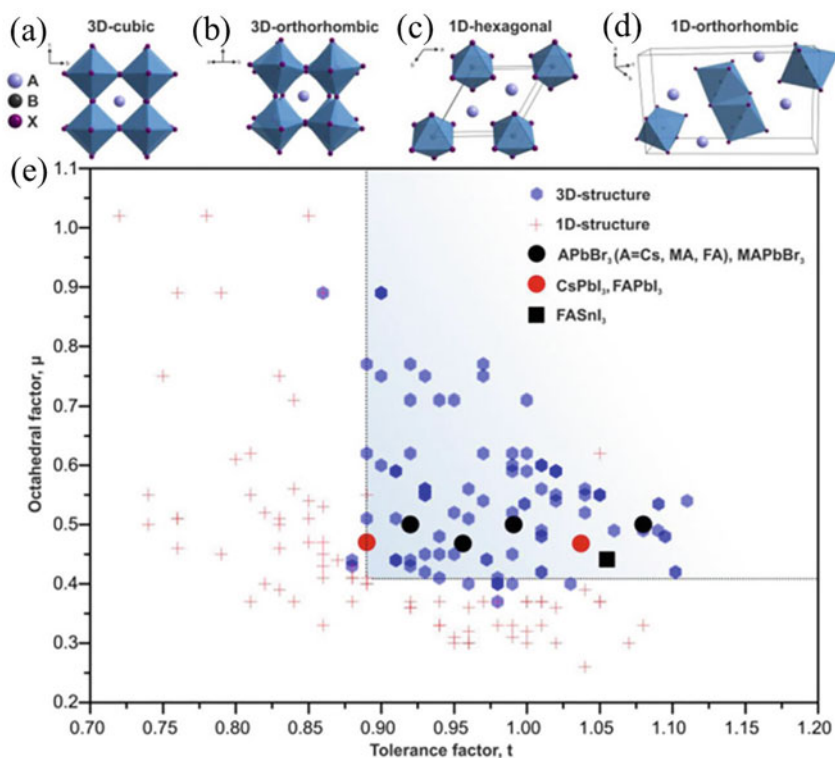


Fig. 1 Illustration of **a** α -FAPbI₃ with ideal 3D cubic structure, **b** CsPbBr₃, an orthorhombically distorted 3D structure, yellow phases of **c** FAPbI₃ and **d** CsPbI₃ with 1D hexagonal lattice and 1D orthorhombic structure, respectively. **e** Octahedral and Tetragonal factors for various 1D and 3D structures of MHPs (both all-inorganic as well as hybrid). The light blue squared area represents the area where the compositions adopt stable perovskite structure at room temperature and pressure [61]

which makes the energy states immune towards external defect levels [65]. Even though the defects states formed in MHPs are mostly benign, a careful investigation of defect physics for the perovskites needs to be carried out.

3 Synthesis Strategies/Methods for MHPs

Various synthesis strategies for high-quality MHP NCs are developed in order to have control over the shape, size, composition without compromising their quality. These strategies are basically divided into two categories, namely, “top-down” or “bottom-up” approaches as illustrated in Fig. 3. Top-down approaches involve ball-milling

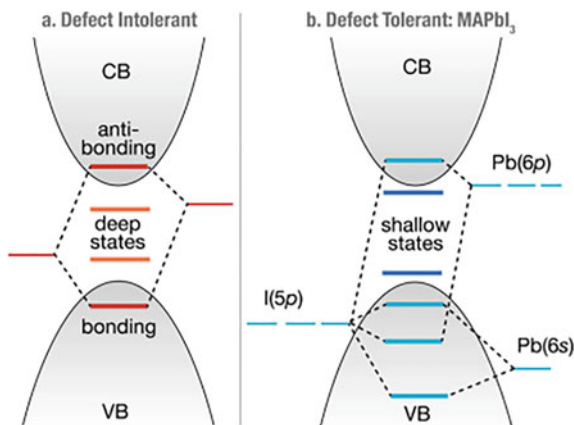


Fig. 2 Electronic structure of **a** a typical defect intolerant semiconductor belonging to III – V, II – VI or group IV and **b** lead-based halide perovskite, MAPbI₃, showing the defect tolerance due to the presence of defect states near the CB and VB edge [65]

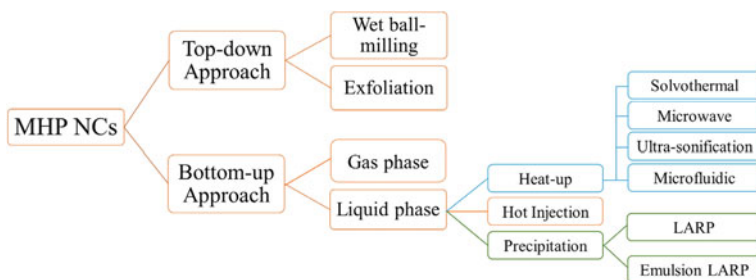


Fig. 3 Flow chart showing the various synthesis methods of nanocrystals of metal halide perovskites

(surfactants are used for size-control), chemical or mechanical (ligand-assisted) exfoliation [30, 66]. Bottom-up approaches mainly use gas- or liquid-phase chemical reactions and are further divided into three main sub-categories: (i) heat-up, (ii) re-precipitation and (iii) in-situ synthesis. In this chapter, we will mainly talk about the frequently used synthetic procedures viz., hot injection (HI) and ligand-assisted reprecipitation (LARP) method for colloidal MHP NCs.

3.1 Hot-Injection (HI) Method: Colloidal Synthesis

In 1993, Murray et al. first reported HI method for the preparation of high-quality cadmium chalcogenide (CdE; E = S, Se, Te) NCs [67]. For the synthesis, the organometallic reagents are heated along with other salts and surfactants in inert

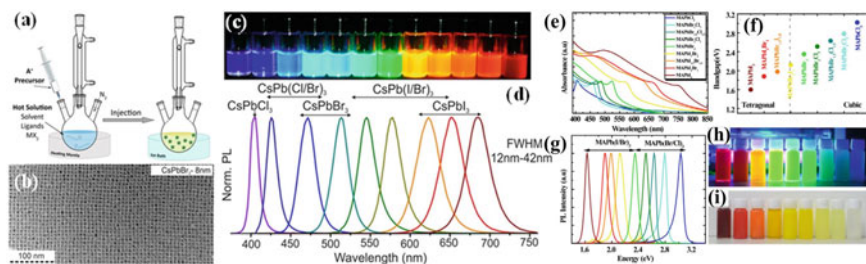


Fig. 4 **a** Hot-injection method for the formation of MHP NCs. **b** Recorded TEM image of uniformly distributed CsPbBr₃ NPs. **c** Digital image of dilute toluene dispersions of colloidal CsPbBr₃ NPs under UV lamp. **d** PL emission spectra of Cs-based perovskite NPs spanning the whole visible range (400–700 nm) obtained by adjusting the halogen ratios [56]. **e** Absorption spectra, **f** bandgap extracted using tau plot and **g** PL spectra of composition-controlled MAPbX₃ nanoparticles using HI method. Digital images of the corresponding samples **h** under UV lamp and **i** in normal light [69]

atmosphere (as illustrated in Fig. 4a). In this method, the nucleation is controlled to grow the highly monodispersed NCs [68]. Injection of precursors to the hot solution rapidly starts the nucleation process followed by the formation of small nuclei. With time, the nuclei start growing and finally contribute to the NC's population. The size, shape and the distribution of NCs can be controlled by varying the ratio of the precursors to the capping surfactants, or the reaction time or the temperature at which the precursor is introduced into the reaction medium. The main benefit of HI method is that it does not use any polar solvent to achieve the successful synthesis of nm-sized materials.

Protesescu et al. utilised the HI method for the successful synthesis of colloidal CsPbX₃, X = Cl, Br and I NCs in 2015 [56]. The method involves dissolving PbX₂ in octadecene (ODE) at high temperature (140–200 °C), where, oleylamine (OLA) and oleic acid (OA) are added in equimolar ratio to ensure the complete dissolution of PbX₂ with an added benefit of stabilizing the NCs in colloidal form. The reaction of PbX₂ in ODE with organic acids at high temperature results in the formation lead-oleate and halide ions. Finally, Cs ions (in the form of Cs-oleate, synthesized using Cs₂CO₃ and OA in the presence of ODE) are injected in the hot solution to obtain CsPbX₃ NCs. This instantaneous injection helps in attaining the uniform distribution of shape and size of the MHP NCs as illustrated in Fig. 4b. The size of the obtained NCs can also be tuned from 5–12 nm by varying temperature of the reaction [56]. The optical characteristics of the as-prepared NCs can be conveniently engineered across the entire visible range of spectrum from 400–700 nm using the HI method by merely adjusting the lead halide ratios (PbCl₂/PbBr₂ or PbBr₂/PbI₂) as observed from Fig. 4c–d. The amines and acids used in HI method play a crucial role in determining shape and size of perovskite NPs. Pan et al. studied the detailed structure and morphology of colloidal perovskite NCs by varying carboxylic acids and amines hydrocarbon chain length [70]. The HI method was modified further to synthesize hybrid organic–inorganic lead-based halide perovskite NCs by replacing Cs-oleate

with MA solution or FA-oleate [71, 72]. Later, the process was utilised to obtain stable blue emitting mixed-halide FAPb(Cl_{1-x}Br_x)₃ NCs [73] and FAPb(I_{1-x}Br_x)₃ NCs with tunable emission ranging from 570 to 780 nm [74]. HI method was further used to fabricate various inorganic perovskites ranging from 3D-CsPbX₃ to 2D-CsPb₂Br₅ and 0D-Cs₄PbBr₆ [75, 76]. The high solubility of colloidal MHP NCs in polar solvents results in a deterioration of their stability in external environmental conditions such as humidity, light, heat, etc., resulting in the loss of their PLQY [53]. In this regard, Yuan et al. showed the sensitivity of perovskite NCs toward different antisolvents used for cleaning [77]. The change in the halide composition of CsPbBr_{1-x}I_x NCs was observed in different antisolvents such as acetone, IPA, n-butanol etc., considerably affecting the optical properties in contrast with pristine CsPbBr₃ NCs. In order to compensate the loss of halide ions in CsPbX₃ NCs, Woo et al. reported fabrication of inorganically passivated (halide-rich condition) perovskite NCs via in situ route [78]. Additionally, the use of metal halide along with PbX₂ precursors resulted in the synthesis of halide-rich compositions which not only prevented the change in optical properties, but, enhanced the ambience stability as well.

The synthesis of composition-controlled MA-based halide perovskites using HI method started in 2015. Unlike Cs and FA precursors, the non-availability of MA-acetate as well as highly volatile nature of MA (boiling temperature of 4 °C) make the use of conventional HI method for their synthesis very difficult. This is the main reason behind storing this molecule in THF or alcohols like ethanol or methanol due to their boiling temperature of around 60–70 °C. Vybornyi et al. demonstrated a modified-HI method to synthesize MAPbBr₃ and MAPbI₃, however, the synthesis of MAPbCl₃ and the (I/Br and Br/Cl) mixed-halide counterparts was still a big challenge [71]. The approach included solubilizing PbX₂ in ODE with a minimal amount of OA and OLA ligands at 120 °C. Next, MA was injected rapidly into the solution after bringing the temperature down to 55 °C to avoid any decomposition. In 2019, Roy et al. utilized this method to obtain the whole series of composition-controlled MAPbX₃ nanoparticles, including MAPbCl₃ in gram scale [69].

3.1.1 Modified HI Method: Overcoming the Limitations of Conventional HI Method

The conventional HI method uses metal halide salt as a source for both cation and anion sites which restricts the use of this method in obtaining desirable ion stoichiometry [56]. The limitation of this method was overcome by introducing a modified, so called, “three-precursor” HI method. In this method, three separate precursors as sources for A cation, lead and halogen sites are taken which in turn helps in achieving and controlling the required lead to halogen ratio. Liu et al., for the first time, synthesised CsPbX₃ (X = halide) NCs using “three-precursor” HI method, where, instead of PbX₂ precursor as a source for lead and halogen, individual reagents NH₄X (halogen-source) and PbO (lead-source) were utilised [79]. Several reports suggest that the NCs synthesised in halide-rich conditions show improved optical properties as the

halogen-stripping is somewhat compensated during the purification process [78]. For instance, CsPbCl₃ NCs synthesised under halide-rich conditions showed near-unity PLQY [28]. The three-precursor HI method was further utilised by Yassitepe et al. in order to eradicate the degradation of the perovskite QDs during the purification process [80]. The degradation is primarily ascribed to the rapid ligand loss due to the proton transfer between OA and OLA surfactants. The authors used quaternary alkylammonium halides as halogen sources (without any need for OLA), thus, synthesizing OA-capped perovskite QDs. This new synthetic route not only enhanced the colloidal stability of the QDs, but also substantially improved the PLQY to up to 70%. Further modification in the three-precursor HI method resulted in the successful synthesis of colloidal FAPbX₃ NCs [72]. The method utilized reaction of acetates of FA and Pb in OA and ODE with oleylammonium bromide, however, the impurity peaks corresponding to NH₄Pb₂Br₅ (probably due to the decomposition of FA⁺ into NH₄⁺) were also present in the final product.

While the three-precursor HI method offers the flexibility to fine-tune the quantity of the different precursors by using individual sources for metal and halide ions and subsequently, achieve the final composition of NCs, the method itself has a few limitations. The modified HI method failed to successfully synthesize CsPbX₃ (X = Cl and I) and MAPbX₃ (X = Br and I) NCs [74]. Additionally, as discussed earlier, due to the decomposition of alkylammonium halide during the synthesis process of FAPbX₃ NCs, substantial amount of impurities were present in the final phase [72]. In order to eliminate these drawbacks, Imran et al. reported the injection of highly reactive halides such as, benzoyl halides, into the solution of metal cations, primarily in carboxylate form for the formation of APbX₃ (A = Cs/MA/FA; X = halide) NCs (Fig. 5a) [81]. The injection induces immediate release of the halide ions which subsequently confirm the evolution of perovskite NCs. The NCs obtained using this method show extraordinary optical properties (narrow PL emission; Fig. 5b, c), uniform size distribution and excellent stability in air without any post-synthesis modifications. The process promotes the partial replacement of Cs ions with the oleylammonium ions, resulting in the lead halide-terminated surfaces, thereby, helping to improve their stability and photophysical properties. In addition, Creutz et al. extended this synthesis approach for the fabrication of lead-free colloidal Cs₂AgBiX₆ (X = halide) NCs using trimethylsilyl (TMS) halides as halogen sources (Fig. 5d–i) [82]. In short, these strategies allow to attain different compositions by adjusting cation or anion ratios, thereby helping in tuning the optical properties and enhancing the relative stability of the NCs.

3.1.2 HI Method: Regulating the Morphology of MHP Nanocrystals

The control on shape and size of both all-inorganic [25, 56] and hybrid organic–inorganic lead-based halide perovskite NCs [20] has been done by regulating reaction time, reaction temperature and compositions in colloidal-based synthesis procedures. After the synthesis of MAPbBr₃ (MA = CH₃NH₃) NCs as initiated by Schmidt et al. [20], the various reports on the synthesis of nanoplatelets of hybrid perovskites show

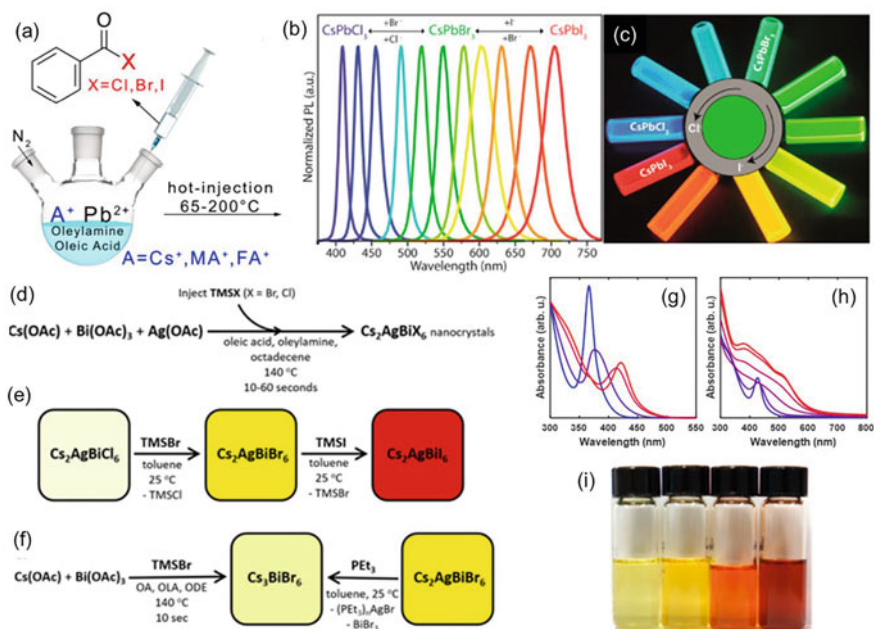


Fig. 5 **a** Schematics for the preparation of lead-based halide perovskite NCs using benzoyl halides as anion precursors utilizing colloidal-based HI method. **b** Evolution of PL spectra via anion-exchange achieved by adding benzoyl iodide or benzoyl chloride to already synthesized $CsPbBr_3$ NCs. **(c)** Digital images of different solutions prepared via anion-exchange reaction under UV lamp [81]. **d-f** Schematics for the synthesis route for Cs_2AgBiX_6 NCs. **g** Absorption spectrum of $Cs_2AgBiCl_6$ NCs (blue) converting to $Cs_2AgBiBr_6$ NCs (red) via anion-exchange mechanism (progressive addition of TMSBr). **h** Absorption spectrum of $Cs_2AgBiBr_6$ NCs (blue) converting to Cs_2AgBiI_6 NCs (red) via anion-exchange mechanism (progressive addition of TMSI). **(i)** Digital images of solutions of $Cs_2AgBiBr_6$, $Cs_2AgBiBr_{5.2}I_{0.8}$, $Cs_2AgBiBr_{1.6}I_{4.4}$, and Cs_2AgBiI_6 NCs in toluene (Left to Right) [82]

tuning of their thickness by varying the organic cations [83]. In case of all-inorganic perovskite NCs, Protesescu et al. reported the first successful synthesis of $CsPbX_3$ ($X = Cl, Br, I$) nanocubes using HI method followed by rapid cooling [31, 56]. Since then, significant advances in the development of MHP NCs resulted in the shape control ranging from nanowires (NWs) [84] to nanorods (NRs) [85] to nanoplatelets (NPLs) [27] and nanocubes [85]. Bekenstein et al. reported the tendency of formation of quasi-2D geometries (known as NPLs) for reactions using OA and OLA carried out at temperatures of $90-130^\circ C$, symmetrical nanocubes at $150^\circ C$, while NWs are preferred at relatively high temperatures of $170-200^\circ C$ [27, 84]. Further, Pan et al. studied in detail the effect of surfactants/ligands on $CsPbBr_3$ NC's morphology [70]. In order to understand this correlation, the chain lengths of the carboxylic acids and alkyl amines used in the reactions were systematically varied. It was observed that shorter length of carboxylic acids (added at $170^\circ C$) favoured the formation of larger-sized nanocubes. Later, in another set of experiments, OA was kept fixed and

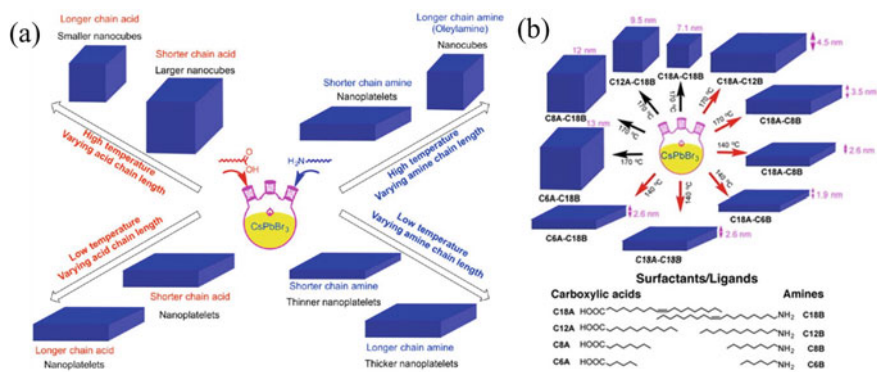


Fig. 6 **a** Schematics showing the correlation between the different morphologies (shape and size) and length of the chain of the amines and carboxylic acids. **b** Controlling the shape and size of NCs using HI method by using different ligands and at different temperatures. Nanocubes are formed at higher temperatures with short length carboxylic acids whereas, thin NPLs result from short length amines. At low temperatures, NPLs are formed using short length carboxylic acids [70].

different alkyl amines at 170 °C were used, resulting in the formation of NPLs (see Fig. 6).

The morphology of perovskite NCs depends significantly on the temperature at which the reaction is conducted. Generally, the precipitation of perovskite precursors leads to the formation of nanocubes at relatively high temperatures, while at low temperatures, formation of NPLs is more likely to occur. This dependence on temperature can be well understood by the protonation or deprotonation of the ligands (alkylamine) controlled by acid or base equilibria during the synthesis process while, Cs⁺ ions compete for their incorporation to the facets during the growth of NCs [86]. Almeida et al. further elucidated the effect of relative concentration of carboxylic acids and alkylamines on the shape, size and distribution of CsPbBr₃ NCs [86]. They reported an increase in the temperature for PbBr₂ precipitation from 195 °C to 290 °C with an increase in the concentration of the ligands. Additionally, the study revealed that low concentration of oleylammonium species tends to form nanocubes (size ranging from 4 nm to 16.4 nm with narrow size distribution) while, the NCs grow anisotropically at higher concentrations (see Fig. 7).

Ultrathin LHP NWs (diameter < 3 nm; down to atomic level) are of current interest due to their strong confinement effects [87]. However, due to the difficulty in controlling the crystal growth at the atomic level, it is very hard to synthesize uniform ultrathin NWs. In 2015, Zhang et al. illustrated the synthesis of CsPbBr₃ NWs using conventional HI method, where, the reaction condition was altered drastically to room temperature (RT) at different intervals of time [84]. It was observed that initially at $t < 10$ min, nanocubes (size varying from 3 to 7 nm) dominated the reaction (Fig. 8). The structure evolved from nanocubes to square-shaped nanosheets (NSs) with fewer thin NWs after around 30 min. After one hour, the reaction was dominated with uniform NWs of diameter below 12 nm and lengths up to several microns.

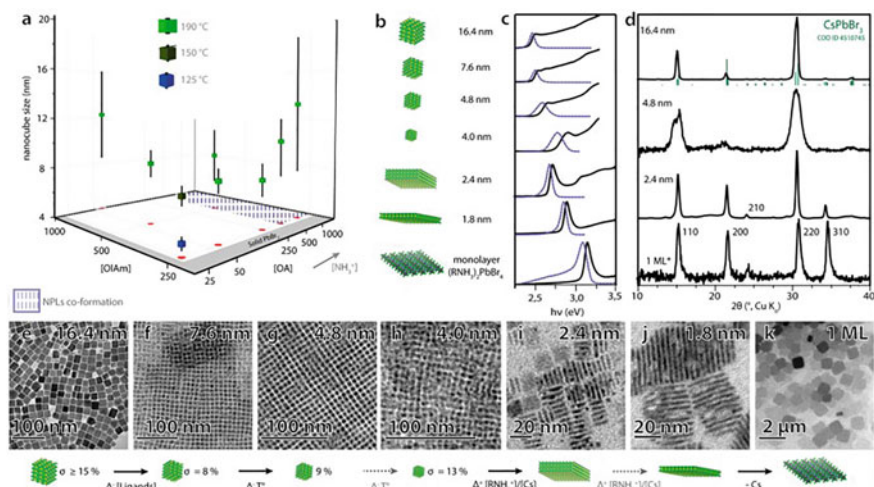


Fig. 7 a Change in OA and OLA concentration and temperature of reaction in order to vary the size of CsPbBr₃ nanocubes (vertical bars denote size distribution). b Drawing of various NCs of CsPbBr₃ attained using OA and OLA ligands only c corresponding absorbance (black lines) and photoluminescence spectra (blue lines) d X-ray diffraction (XRD) profiles and e–k TEM images [86]

Further in 2016, Zhang et al. worked on improving the quality and yield of ultrathin perovskite NWs (2.2 ± 0.2 nm width) showing a blue shift in PL (~ 465 nm) as compared to the bulk counterpart (~ 530 nm) [87]. Further reports on the modification of perovskite NWs (reduction in dimension up to quantum confinement regime) suggest the incorporation of carboxylic acids with short chain lengths in addition to OA and OLA [23].

Even though HI method has been used successfully for the fabrication as well as gaining control on the shape and size of LHP NCs, the method is tedious and requires inert conditions. Moreover, an additional step is needed in order to prepare Cs or FA oleate which are again heated just before the injection which makes the procedure arduous. Also, large scale production using HI method is difficult as precursors used in large quantities result in remarkable drop in the reaction temperature which encourages inhomogeneous nucleation [56]. Various alternative approaches

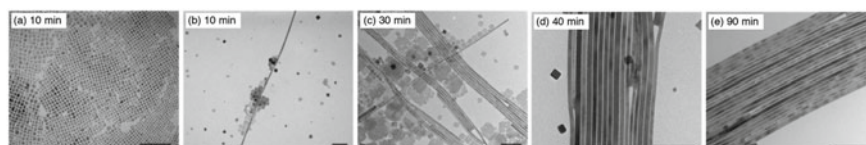


Fig. 8 Evolution of shape of CsPbBr₃ NCs as a result of different reaction times [84]

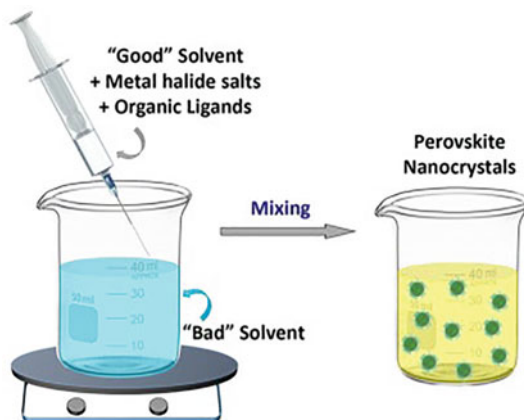
like ligand-assisted reprecipitation technique, ultrasonication, microwave irradiation, solvothermal method etc. have been employed in order to overcome the above mentioned drawbacks of HI method [88–91].

3.2 Ligand-Assisted Reprecipitation (LARP) Method

The process of reprecipitation stems from recrystallization of salts in clay pots back in 3500 BC in South Poland [85]. The process is simple and involves first dissolving all the precursor ions into a suitable solvent until an equilibrium state is reached. Then, the equilibrium state is disturbed by means of either evaporating the solvent or changing the temperature or by moving the solution into an anti-solvent. These conditions trigger a spontaneous precipitation and the crystallization happens until the equilibrium state is reached once again. The process can also be used to prepare nanoparticles, by carrying out the reaction in the presence of surfactants or ligands, that is why the name “ligand-assisted” reprecipitation is used, where, the crystals in the nm range can be grown (see Fig. 9).

The formation of MHP NCs using LARP method involves the dissolution of initial lead-halide (PbX_2) and BX (B = Cs, MA and FA) salts in a polar solvent like dimethylsulfoxide (DMSO), dimethylformamide (DMF) etc. In a different beaker, a poor (bad) solvent (in which the precursor ions are not soluble) such as hexane, toluene etc., is taken along with the ligands. When the two solutions are mixed together, a spontaneous supersaturation causes the nucleation and growth of LHP NCs. Unlike HI method, the whole reaction is carried out in open atmosphere and at room temperature. In HI method, the reaction temperature controls the size of nanocrystals and variation in temperature upon injection of the precursor solution hampers the reproducibility of NCs [92]. This affects the mass production (gram scale) of perovskite NCs and is resolved by LARP method, a RT-based synthetic

Fig. 9 Illustration of LARP synthesis method [85]



approach [92, 93]. In 2012, Papavassiliou utilized LARP method for the development of various lead-based perovskites which includes MAPbX₃ and other MA-based layered materials with Pb_n(Br_xCl_{1-x})_{3n+1}, Pb_n(Br_xI_{1-x})_{3n+1}, and Pb_n(Cl_xI_{1-x})_{3n+1} (n > 2) units [94]. Only after a few years of rigorous efforts, LARP method was extended to prepare NCs of all-inorganic as well as hybrid halide perovskites, ABX₃, where B belongs to Pb, Bi, Sb or Sn [47, 85].

3.2.1 Synthesis of Hybrid and All-Inorganic Lead-Based Halide Perovskite NCs Using LARP Method

LARP method for the preparation of perovskite NCs in ambient conditions utilizes the inherent ionic nature of perovskites. In 2015, Zhang et al. prepared highly luminescent MAPbBr₃ NCs using LARP method for the first time (Fig. 10a–c) [22]. The NCs were obtained by preparing a clear precursor solution in DMF containing OLA and OA (surfactants). A suitable amount of this solution was added dropwise into toluene and vigorously stirred at RT resulting in the formation of a yellow-green colloidal solution which was further cleaned to obtain high-quality MAPbBr₃ nanoparticles. The work involved further exploration of the role of carboxylic acids and alkyl amines, where, they demonstrated the loss of control on the size of the crystals in the absence of amines. On the other hand, aggregated NCs were formed when carboxylic acids were not used. It was concluded that amines help in regulating the size of NCs (kinetics of crystallization) whereas, carboxylic acids help in preventing the aggregation of NCs and was followed by many other groups [95, 96]. Additionally, the heating of toluene controls the size of MAPbBr₃ NCs and their distribution, as suggested by Huang and his co-workers [95]. Further, the modified LARP method involves the formation of MAX salt in situ without the effort to make it individually [97]. In a conventional procedure, PbX₂ was dissolved in N-methylformamide (NMF; acting as a solvent as well as a source for MA⁺ ions) instead of DMF along with OA and OLA at 100 °C for 10 min (Fig. 10d). Afterwards, the solution was dropped into chloroform at RT to yield MAPbX₃ (X = Br and I) NCs. The bulk MAPbX₃ crystals can also be produced using this technique at RT with no antisolvent.

Levchuk and co-workers reported the synthesis of FAPbX₃ (X = Cl, Br and I) NCs (Fig. 10e–f), where, the precursor solution of FAX and PbX₂ in DMF, OLA and OA were injected rapidly into chloroform instead of toluene at RT [98]. The study showed the prevention of formation of FAPbI₃ NCs and immediate agglomeration of FAPbBr(Cl)₃ NCs. The synthesis of colloidal all-inorganic CsPbX₃ NCs at RT using LARP method resembled that for MAPbX₃ NCs. Li et al. used the solution of inorganic salts PbX₂ and CsX in DMF, OA and OLA and mixed dropwise in toluene to obtain CsPbX₃ NCs (Fig. 10g–i) [89, 99].

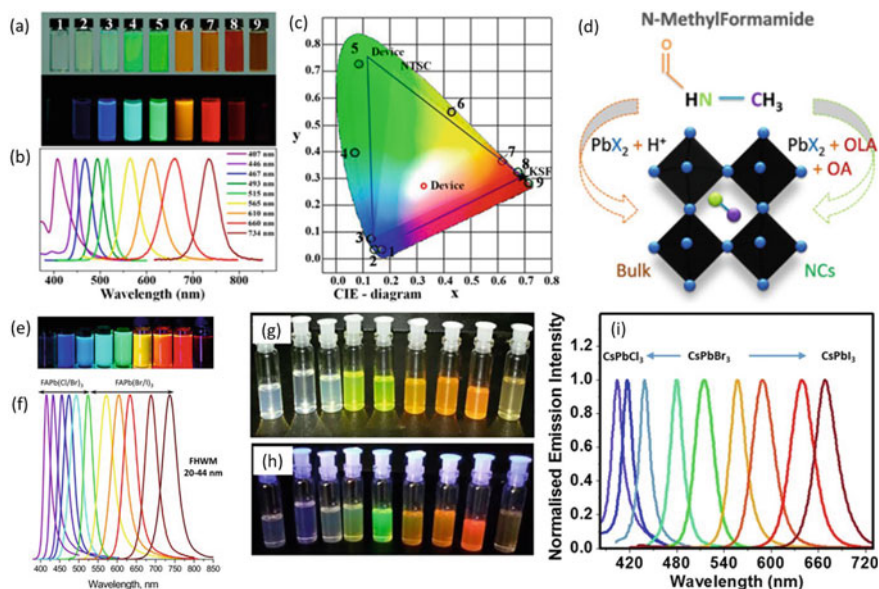


Fig. 10 **a** Digital images of MAPbX_3 ($X = \text{Cl}/\text{Br}/\text{I}$ or their halide mixtures) NCs under ambient light and a UV lamp ($\lambda = 365 \text{ nm}$). **b** Photoluminescence spectra taken for MAPbX_3 NCs. **c** Corresponding CIE color coordinates [22]. **d** N-methyl formamide (NMF) acts as a source of MA^+ ions and solvent for the synthesis of both bulk- and nano-crystals MAPbX_3 . [97] **e** Digital images of colloidal solution of FAPbX_3 ($X = \text{Cl}/\text{Br}/\text{I}$ or their mixture) NCs in toluene under a UV lamp. **f** Corresponding photoluminescence spectra showing the compositional tuning [98]. Digital images of all-inorganic CsPbX_3 NCs under **g** ambient light, **h** a UV lamp and **i** their corresponding PL spectra [99]

3.2.2 LARP Method for Controlling the Shape and Size of MHP NCs

After the successful synthesis of MHP NCs using LARP method, several research groups worked towards controlling their shape and size in order to optimize the PL emission. For instance, in 2015, Sichert and team demonstrated the control on the thickness of MAPbBr_3 NPLs which resulted in change of the PL emission by varying the ratio of the organic cations (octylammonium (OA^+) and MA^+) used [101]. The thickness of the NPLs decreases with the systematic increase in OA/MA ratio with “single-layered” NPLs obtained on using OABr only. Other reports also suggest the similar observation of obtaining monolayer thick NPLs using octylamine and OA [102]. Moreover, the transformation from 3D nanocubes to 2D nanostructures can be achieved by adding pyridine during the growth of NCs (Fig. 11a) [100]. The pyridine in the solution binds selectively to the MAPbBr_3 surface and promotes 2D growth due to the formation of native $\text{N} \rightarrow \text{Pb}$ bonds which restricts the vertical growth. Figure 11b–g shows the effect of variation of temperature on the thickness of these 2D-nanostructures resulting in the formation of $n \approx 2$ (face-stacking NPLs), $n \approx 4$ (thin sheets) and $n \approx 6$ (quasi-2D nanostructures), where, n is the number

of layers of the unit cell. Kirakosyan et al. achieved the lateral size reduction of the MAPbBr₃ NCs by slowly changing the quantity of the precursor solution at a constant rate to the anti-solvent which results in the reduction from 3 to 8 nm without altering the thickness (~3 nm) of the NCs [103]. Levchuk et al. varied OA to OLA ratio in order to fine tune the thickness of the MAPbX₃ (X = Br and I) NPLs down to the quantum confinement regime [104]. By adjusting the thickness of the NPLs only, the PL emission was tuned from 450 to 730 nm with pronounced quantum size effect (thickness ≤ 2.2 nm; 3D Bohr radius in MAPbBr₃ perovskites). Later, they utilised the same technique with some minor modifications to obtain FAPbX₃ NCs (use of chloroform instead of toluene); change in OA/OLA ratio resulted in the formation of different morphologies with different thickness (see Fig. 11h–l) [98]. Seth and co-workers demonstrated the formation as well as the sequential evolution of different morphologies (QDs, NPLs, nanocubes, NRs and NWs) of high-quality CsPbX₃ NCs just by varying the reaction parameters [99]. It was observed that on using ethyl acetate as anti-solvent, quasi-cubic CsPbBr₃ QDs (Fig. 11o–p) were formed immediately. On increasing the reaction time to 10 min, a few layered thick square-shaped NPLs were obtained which transformed to nanobars after increasing the reaction time further to 40 h (Fig. 11q–r). This is attributed to the high polarity of ethyl acetate as compared to toluene which enables it to work as a nucleophile causing the detachment of some OLA molecules from nuclei surface and results in an oriented attachment (Fig. 11m). The size of these nanocubes were further altered (edge length varying from ~12 nm to 34 nm) by using toluene as anti-solvent while keeping OA and OLA as ligands. However, at lower concentration of OLA, the formation of NRs (length = 800 nm and diameter = 70 nm) was observed which eventually transformed to NWs (diameter ~70 nm and length ≥ 15 μm) with increase in reaction time (Fig. 11s–v)). This is because in case of toluene, at lower concentration of OLA, the surface of NCs is not fully protected in all directions and the anisotropic growth of NCs (formation of NWs/NRs) happens when the reaction is carried out for prolonged duration, as seen from Fig. 11n.

3.2.3 Limitations of LARP Method

Apart from the advantage of direct synthesis of perovskite NCs in open environment without any heat treatment, the LARP method has certain limitations. LARP method makes use of the polar solvents like DMSO, DMF etc., which can possibly degrade or even solubilize the final product [92, 106]. The interaction between precursor and polar solvents played an important part in forming defective LHP NCs. In this context, Zhang et al. studied these interactions as well as demonstrated the influence of various polar solvents on the crystallization of MAPbI₃ NCs [105]. It was observed that the use of coordinating solvents (forming strong intermediates with PbI₂) such as, DMF, DMSO and tetrahydrofuran (THF) led to the formation of MAPbI₃ NCs with residual solvent still present on the surface of these NCs. The removal of these solvents might create the intrinsic iodine vacancies resulting in the formation of defective NCs which

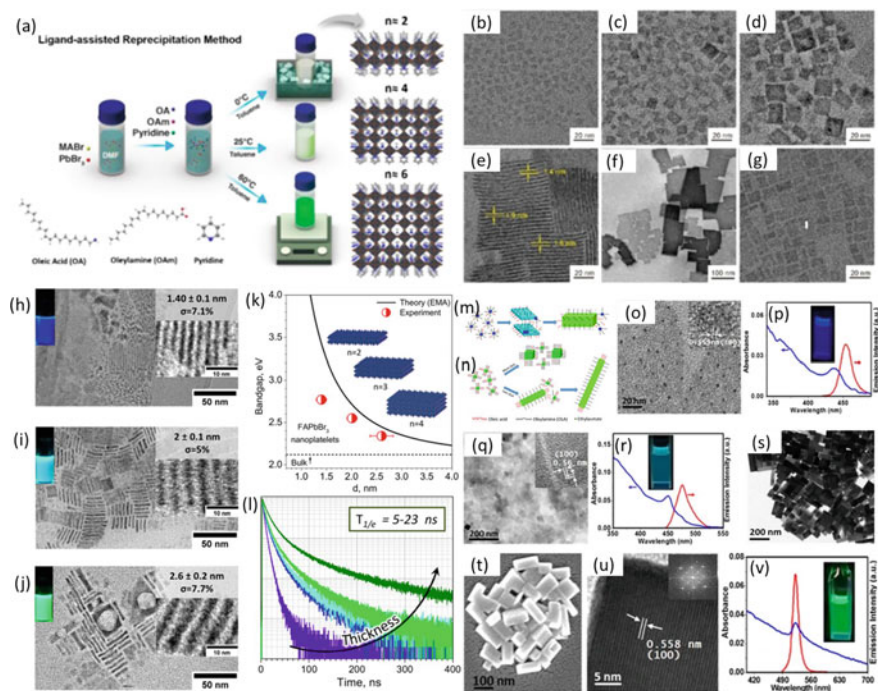


Fig. 11 **a** Illustration for the synthesis of MAPbBr₃ NCs using LARP method using OA, OLA and pyridine resulting in the reduction of 3D nanocubes to 2D nanostructures. TEM images of the corresponding nanostructures obtained at **b** 0 °C **c** 25 °C and **d** 60 °C without pyridine and at **e** 0 °C **f** 25 °C and **g** 60 °C after addition of pyridine [100]. TEM images of thickness-controlled FAPbBr₃ NCs prepared by varying OLA/OA ratio keeping amount of OLA fixed at 200 μl and varying OA to **h** 150 μl, **i** 80 μl and **j** 40 μl (inset shows the emission of different FAPbBr₃ NPLs; σ = thickness distribution). **k** Comparison between experimental and theoretical bandgap as a function of thickness, *d*. **l** PL decay [98]. Formation mechanism for (m) NPLs (cyan) and nanobars (green) and **n** larger nanocubes, NRs and NWs from smaller nanocubes in ethyl acetate and toluene, respectively. **o** TEM image and **p** absorption and PL spectra of CsPbBr₃ QDs. **q** TEM image and **r** absorption and PL spectra of CsPbBr₃ NPLs. **s** TEM image, **t** FESEM, **u** HR-TEM and **v** absorption and PL spectra of CsPbBr₃ nanobars [99]

probably convert to MAPbI₃·H₂O intermediate due to the water present in the solvent or air (turbid solution as seen in Fig. 12) [105].

3.3 Alternate Approaches for the Synthesis of LHP NCs

Various other chemical-based approaches such as solvothermal method, microwave irradiation, ultrasonication etc. as well as non-chemical-based approaches like

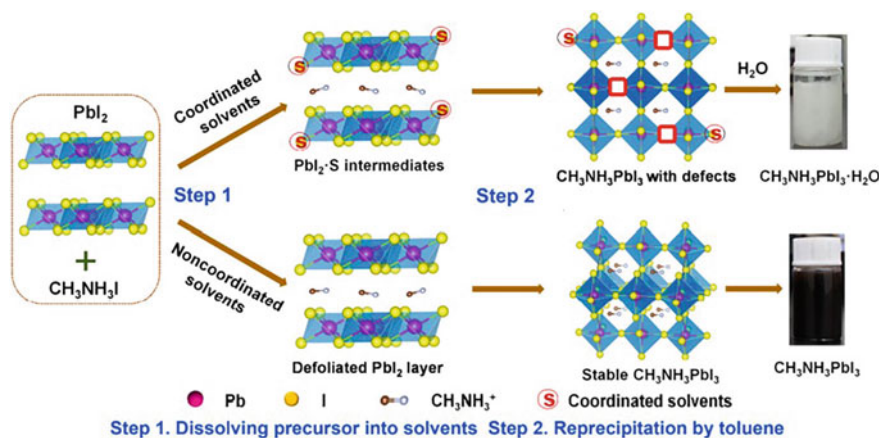


Fig. 12 Effect of the coordinating and non-coordinating solvents on the crystal structure of MAPbI₃ NCs [105]

mechanochemical method have also been investigated by various research groups for the synthesis of perovskite NCs [88, 90, 91, 107].

Chemical-based Approaches: Chen et al. used *solvothermal method* to synthesize CsPbX₃ NCs with tunable optical properties [88]. The process involved sealing stoichiometric amount of cesium acetate and PbX₂ salt dissolved in octadecene (ODE) along with ligands, OLA and OA in a stainless autoclave. The system is then heated at high temperatures of 140–200 °C in an oven for 30 min. Using this method, monodisperse nanocubes of CsPbX₃ NCs were prepared together with the successful control on the composition where, X is Cl, Br, I or their mixture and bright PL emission spanning the whole visible range. Furthermore, simply pre-dissolving the precursors in ODE using magnetic stirring, the morphology can surprisingly be changed from CsPbBr₃ nanocubes (green emission) to ultrathin CsPbBr₃ NWs with a diameter of ≈ 2.6 nm, giving a blue emission confirming the quantum confinement effect (Fig. 13a). The method was further extended by Praveen and co-workers to obtain the composition-controlled MAPbX₃ nanosheets with variable thickness resulting in a tunable emission down to the quantum confinement regime [108]. Another strategy, namely, *microwave irradiation* was also utilised by Pan et al. in order to control the halogen composition of CsPbX₃ NCs [90]. The process included mixing Cesium acetate, PbX₂, OA, OLA, trioctylphosphine oxide (TOPO) and ODE in a quartz tube which is then placed in a microwave reactor at 160 °C (28 °C/min) for 5 min. The use of TOPO helped in producing high-quality NCs by preventing the agglomeration of the precursors. The control on different morphologies viz., nanocubes, NPLs and NRs can also be achieved using this method (Fig. 13b). By reducing the reaction temperature from 160 °C down to 80 °C, the plate-like CsPbBr₃ NCs were obtained. Further, if the precursors were pre-dissolved before microwave treatment, just like in solvothermal method, rod-like morphology of CsPbBr₃ NCs was achieved. The minor modification of separating the nucleation step (addition of IPA to the solution

of Cesium oleate and PbBr_2) from the growth step (when microwave irradiation is turned on) in the microwave-assisted method was done by Shamsi et al. in order to obtain the quantum-confined blue-emitting CsPbBr_3 NPLs [93]. Ultrasonic irradiation in place of a microwave treatment as a source of excitation was employed by Tong et al. to synthesize CsPbX_3 ($X = \text{Cl}, \text{Br}, \text{I}$ or their mixture) perovskite NCs with successful control on the halogen composition, thickness and morphology of the NCs (Fig. 13c–g) [91]. Roy et al. utilized the ultrasonic vibration as an excitation source for the synthesis of hybrid mixed halide compound-phase perovskite nanoparticles, $\text{MAPbX}_{3-n}\text{Y}_n$ ($X/Y = \text{I}, \text{Br}, \text{or Cl}$), by mixing two pure-phase perovskites viz., MAPbX_3 and MAPbY_3 [107].

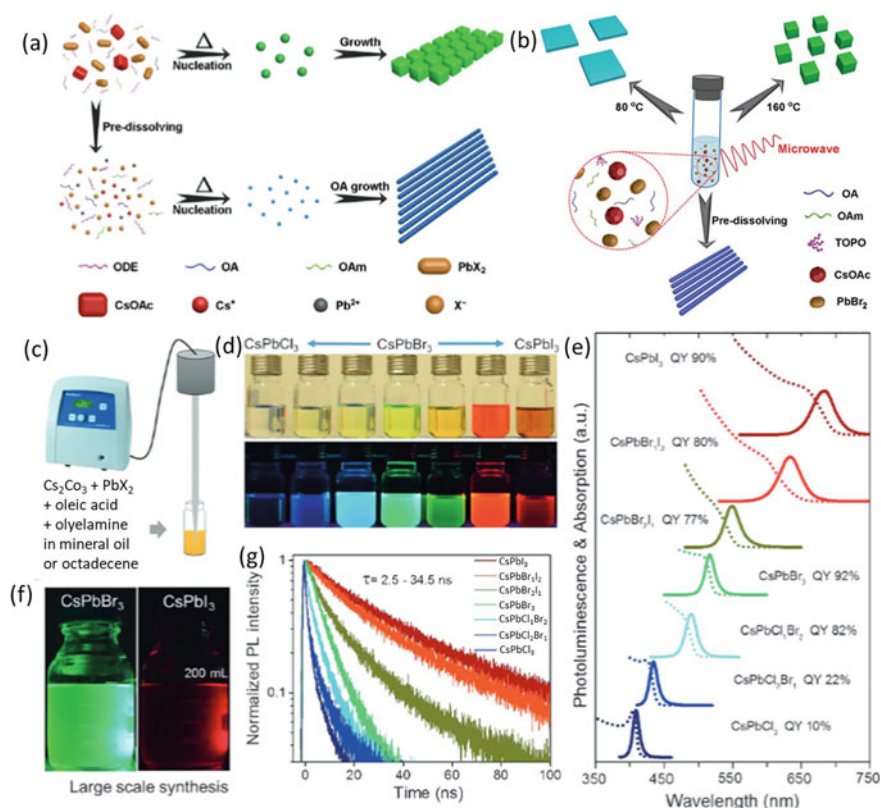
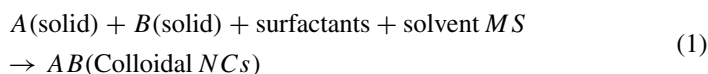


Fig. 13 **a** Schematics illustrating the growth process of NCs using solvothermal method with and without pre-dissolving the precursors [88]. **b** Proposed growth mechanism using microwave treatment. Different morphologies viz., NPLs and nanocubes of CsPbBr_3 are obtained at 80 °C and 160 °C, respectively without pre-dissolving the precursors however, pre-dissolving the precursors resulted in the formation of CsPbBr_3 NRs [90]. **c** Ultrasonication method for preparation of CsPbX_3 NCs. **d** Digital images of CsPbX_3 NCs with different halogen composition in ambient light (up) and under UV lamp (down) and their corresponding **e** optical absorption (dashed lines) and PL (solid lines) spectra. **f** Large-scale production using this technique (up to 10 times). **g** PL decay [91]

Non-chemical-based Approaches: Mechanochemical approach where, mechanical energy is utilized to trigger the chemical reagents, has several advantages over the conventional wet chemical methods. The process is completely solvent-free (volatile solvents are used), cost-effective and can be used for the mass-production of great quality and phase-pure perovskites. Furthermore, several researches show the perovskites synthesised using mechanochemical method show greater stability as compared with the polar-solvent based conventional methods [109, 110]. In a typical process, the weighed perovskite precursors PbX_2 and AX together with long-chain ammonium halide salts are mixed in a mortar-pestle (hand-grinding) or ball-milling. Ball-milling is considered a better method for upscaling as hand-grinding is tedious and generally leads to impure phase. In ball-milling, precursor salts are taken in a stainless-steel jar, where, the mixing is done using the several balls (made of zirconia, agate or corundum). After sealing the jar, it is mounted on a motor where, two movements viz., rotation around the centre of the disk and around its own axis, are performed (Fig. 14a). Consequently, the tossing and collision with the reactant species provides enough energy for the synthesis of desired perovskite phase [66, 110]. The synthesis of NCs using mechanochemical synthesis (MS) approach is done by using surfactants and a volatile solvent in addition to the precursor salts for the reduction of the size as shown below:



However, the first report on the synthesis of $MAPbX_3$ using mechanochemical approach by Hintermayr et al. was based on two-step process [30]. First, grinding

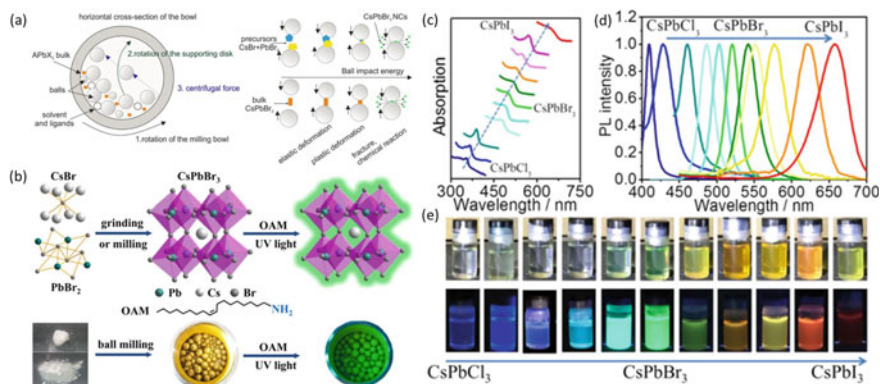


Fig. 14 **a** Illustration showing the working of a ball-mill where the horizontal cross-section of the jar is shown which undergoes two kinds of rotation; one about its own axis and another around the centre of the disk [66]. **b** Illustration for mechanochemical synthesis of $CsPbX_3$ QDs (top) and fluorescence shown by the samples under UV lamp (down). The corresponding **c** UV-Vis absorption and **d** PL spectra of composition-controlled $CsPbX_3$ QDs and their **e** digital images in ambient light (top) and under UV lamp (down) [111]

of the equimolar precursor salts in mortar-pestle for several mins was done to ensure the complete formation of bulk perovskite phase. Next, the perovskite powder was dispersed in toluene and OLA (ligands for size reduction) and sonicated for 30 min to obtain homogenous dispersion. Further, the excess ligands were removed using centrifugation which resulted in the formation of polydisperse rectangular NCs with size ranging from few tens to hundreds of nanometers. Similarly, a full range of CsPbX_3 NCs were obtained using this two-step process by Zhu and co-workers [111]. However, instead of using ultrasonic vibration for the second step, the bulk powder together with surfactants (without any solvent) was ground using ball-milling to obtain the composition-controlled all-inorganic perovskite NCs. Also, instead of bifurcating the process in two steps, perovskite NCs can be directly prepared by grinding the precursor salts in the presence of ligands and solvent, commonly known as liquid-assisted grinding (LAG) [112]. Protesescu et al. extended this method to synthesize hybrid FAPbBr_3 , inorganic CsPbBr_3 and mixed halide $\text{CsPb}(\text{Br/I})_3$ NCs via mechanically induced anion-exchange process [111]. The study also rendered the fact that prolonged milling produced quantum-confined perovskite nanoparticles.

4 Defect Physics in Halide Perovskites

4.1 Defects in Semiconductors: An Overview

Defects are present in all semiconductors, either by accident or by design. A Wide range of applications get affected because of the existence of defects such as, impurities or native defects introduced during the growth and processing of the semiconducting materials [113]. It is very important to understand the energy states for the occupation of electrons and the band structure of semiconductors in order to gain deep insight about the defects. Introduction of impurities during the fabrication or growth process and the lattice imperfections give rise to the energy states in the energy gap between VB and CB, commonly known as defect states. As discussed previously, shallow defects are mostly benign and correspond to the states present within a range of few tens of meV from the respective band edges. On the other hand, deep defects, as the name suggests, penetrate deeply into the energy bandgap and affect majorly the optical and electronic properties of the material [114]. In a typical semiconductor, charge carriers are generated after photo-excitation. Equation 2 shows the charge carriers' recombination as:

$$dt/dn = k_1n_1 + k_2n_2 + k_3n_3 \quad (2)$$

Here, n represents the charge carrier density and k_1 , k_2 and k_3 defines the rate constant for the three different kinds of recombination. The monomolecular recombination, as defined by k_1 , is mainly associated with either excitonic (where electrons and holes are bound by coulombic interactions) or trap-assisted recombination (when

charge carrier gets captured in a trap) and is directly proportional to the charge carrier density, n . The rate constant k_1 , , represents non-radiative recombination and is undesirable for photovoltaic application. The second kind of recombination is known as bimolecular recombination (rate constant, k_2) and is dependent on the density of both the charge carriers viz., electrons and holes, therefore is proportional to n [2] and corresponds to radiative recombination (resulting in luminescence). The rate constant k_3 is associated with Auger recombination (a three-particle process). It is a non-radiative process which includes the transfer of energy gained from charge carriers' recombination to electrons (or holes) which are then excited to higher states.

Shockley-Read Hall (SRH) theory describes the non-radiative recombination, R , mediated through defect states and is given by [115]:

$$R = \frac{n_e n_h - n_i^2}{T_h \left(n_e + N_c \exp\left(-\frac{E_c - E_T}{k_B T}\right)\right) + T_e \left(n_h + N_v \exp\left(-\frac{E_T - E_v}{k_B T}\right)\right)} \quad (3)$$

Here, n_e , n_h and n_i stands for electron, hole and intrinsic carrier density. T stands for lifetime, E_C (E_V) for the CB (VB) energy and N_C (N_V) for the effective density of states DOS of CB (VB). k_B is Boltzmann constant and E_T denotes defect energy level.

Assuming, $n_e \approx n_h \gg n_i$,

$$R = n2T \quad (4)$$

$$T\alpha \frac{1}{N_T \sigma_T} \quad (5)$$

where, N_T and σ_T are number of traps and capture cross-section, respectively.

In case of lead-based halide perovskites, due to the high ability of MAPbI_3 to screen charge (high dielectric constant), σ_T is low and low N_T enables halide perovskites to have long carrier lifetime, making them suitable absorbing material for photovoltaics [116].

4.2 Halide Perovskites and Defects

In past few years, LHPs have revolutionized the photovoltaic and optoelectronic industry because of their excellent optoelectronic properties with added benefit of lower fabrication costs among other semiconductors. Particularly, Cs-based lead halide perovskite NCs, due to high stability and PLQY, are receiving great attention for their potential in display and light-emitting technologies [117, 118]. Though the LHPs are defect-tolerant, the synthesis conditions (reaction temperature, halide rich/poor conditions etc.) often promote the formation of defect states (both for bulk as well as NCs) as evident from their PLQY values which is far from unity

[28, 29]. The defects in crystalline semiconductors can mainly be characterized as crystallographic defects (imperfections in the crystal lattice such as vacancy, anti-site, interstitial, dislocation etc.) and impurities (addition of any foreign elements in the structure). The measured density of defects in bulk LHPs fall in the range of 10^{11} – 10^{16} per cm^3 while, this value drops to one defect in $\sim 10^2$ – 10^7 for a 10 nm perovskite NC, which is too low to explain significant loss in PL efficiency in NCs [119, 120]. The formation of defects at nanoscale is quite different from that in bulk mainly because of the two reasons: (a) the presence of surfactants on the surface of NCs creates a different environment for the defects than in bulk and (b) due to large number of surface atoms, the defects are mostly present on the surface of the NCs than in the bulk [120]. During the washing of NCs, the surfactants can detach from the surface of NCs which might result in aggregation and precipitation of NCs and exposing the surface to defects [70, 120]. Furthermore, in case of NCs (with size in the range 8–10 nm), the defects formed in the bulk/core of the material might eventually travel to the surface, resulting in the formation of the trapping sites for the charge carriers at the surface. This is also seen in perovskite thin films based solar cells where, the loss in efficiency is majorly because of the carrier recombination at the grain boundaries. Also, the structural defects arising from the deviation of an atom(s) from the designated position in an ideal periodic crystal lattice introduces the disorder into the lattice affecting the mobility of free charge carriers as demonstrated in Fig. 15a [121]. Here, in addition to the carrier transport bands, localized electronic states are formed as a result of crystalline imperfections which act as trapping sites for photogenerated charge carriers (Fig. 15b). Depending upon the nature of the trap, the carriers can trace back to the CB by gaining energy either from further optical excitations or through thermal energy at RT ($k_B T \sim 26$ meV). As discussed earlier as well, the defect levels just above the CB and VB edges are benign (shallow defects), whereas, those residing in between the CB and VB edges (deep defects) are harmful as they can trap the charges. The difference in energy between the transport states and the defect levels is known as the trap depth (ΔE). As seen from Fig. 15c, for shallow traps, $\Delta E \leq k_B T$ (very small) and the mobility of free charge carriers are restricted only through trapping/detrapping processes. On the other hand, deep traps are found in the middle of the energy gap with $\Delta E > k_B T$ and accelerate non-radiative recombination by hindering detrapping processes. The formation of these disorders or defects affect adversely the PCE of photovoltaic or optoelectronic devices.

4.2.1 Theoretical Perspective on the Native Defects in MHPs

In order to gain further insights about the defect chemistry of NCs, DFT calculations turned out to be a powerful tool. Brinck et al. employed DFT simulation to compute the defect formation energies (DFEs) of vacancy, antisite and interstitial defects in different regions of NCs [120]. For this, the basic difference between the defect theory for bulk and NCs need to be investigated for better understanding of how these defect/trap states can be suppressed to prevent crystal degradation [45, 120]. Studies show that the interstitial defects are energetically more favourable than the

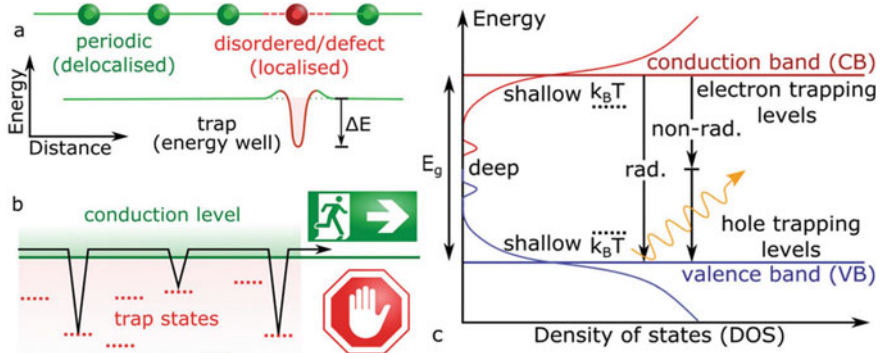


Fig. 15 **a** Schematic diagram of localized defects formed due to the structural defects in the semiconductor (top) and the energy levels introduced by these defects (bottom). **b** Trapping and detrapping processes slow down the transport of free charge carriers. **c** Density of states show the formation of shallow and deep defects with the corresponding radiative and non-radiative recombination in a disordered semiconductor [121]

vacancies and antisites which require large formation energies. However, interstitials only favour the formation of shallow trap states and do not have adverse effect on the material. On the other hand, vacancies result in the formation of deep traps. The density of these vacancies should be very high in order to actually transform them into trap states due to the high defect tolerance of perovskite structure. Experimentally, formation of these defect levels is evident due to the detachment of ligands/surfactants during the purification processes [122].

In this section, we will mainly focus on the defect formation in CsPbBr₃ NCs because of their high phase stability, optical purity and great tolerance against surface treatments [120]. For bulk systems, DFE is simulated using the following equation:

$$DFE(\alpha, q) = E(\alpha, q) - E(bulk) - \sum_A n_A \mu_A + q(E_F + E_{VBM} + \Delta V) + E^q \quad (6)$$

where, $E(bulk)$ and $E(\alpha, q)$ are the total energy of the pristine supercell and supercell with defect α and charge q , respectively; n_A and μ_A are the number and chemical potentials of the atom added/subtracted to form the defect; E_F is the Fermi energy; ΔV is the defect-induced electrostatic shift; E_{VBM} is the energy corresponding to the valence band maxima and E^q is the background electrostatic charge [123].

The accuracy of the DFE largely depends on choices of different exchange–correlation functionals e.g., semilocal, GW and hybrid along with or without spin–orbit coupling (soc) mostly for the correct estimation of the band edge energies [124]. However, this method is not effective for the NC systems as the perovskite NCs are dispersed in solution during the synthesis process. This results in the formation of the molecular ion pairs, viz., PbBr₂ and CsBr which further promotes the creation of the vacancy or interstitial defects in NCs. For instance, during dispersion, detachment of

PbBr₂ ion pair result in the formation of Pb vacancy (V_{Pb}²⁻). Additionally, the Br⁻ ions are also removed from the lattice during the formation of lead vacancy therefore, the correct description for the defect is given by V_{Pb}²⁻ + 2V_{Br}⁺. In NC model, the DFEs are calculated using the simplified equation given as follows:

$$DFE(\alpha) = E(NC(\alpha)) - E(NC) \pm E(s) \tag{7}$$

where, $E(s)$ is the energy of neutral ion pairs (e.g., PbBr₂) and $E(NC)$ and $E(NC(\alpha))$ are the total energies of the pristine NC and NC with defect α (referred to V_{Pb}²⁻ + 2V_{Br}⁺ here). The DFE calculation in NC model take care of the charge neutrality as well as the background charge correction because of the explicit inclusion of the whole NC.

In the CsPbBr₃ NC, three different combination of defects/counterion (needed to neutralize the charge) are investigated: (a) core (c)/surface, (b) surface-centre (sc)/surface and (c) surface-edge (se)/surface. All the cases mentioned here show the energetically favourable formation of interstitial positions, as evident from Fig. 16. This implies that the addition of CsBr/PbBr₂ ion pairs in the lattice is energetically favourable and leads to the formation of interstitial sites (Fig. 17a–b). Experimentally, this infers the easy accommodation of metal salts from the environment, if available. Now, among the different interstitial sites, surface edge is usually more preferable than core. It is important to note that the addition of halide (counterion) results in the emergence of mid-band states irrespective of the cationic/anionic interstitial defects. Further, the formation of deep trap state is favoured by the occupancy of halide anion at the surface positions rather than the core. The creation of trap states is attributed to the dangling and non-bonding lone pairs of the excess halide present at the surface sites.

Removal of ions from the surface or the core results in the formation of vacancies, while the excess counterions need to be removed from the surface to neutralize the

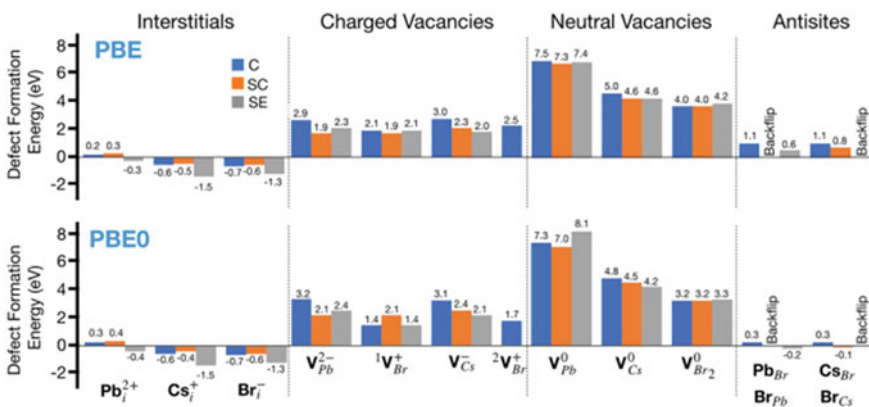


Fig. 16 DFE for interstitials, charged, neutral vacancies and antisite substitutions. All the DFEs are simulated using PBE/PBE0 (Perdew-Burke-Ernzerhof) exchange–correlation functionals [120]

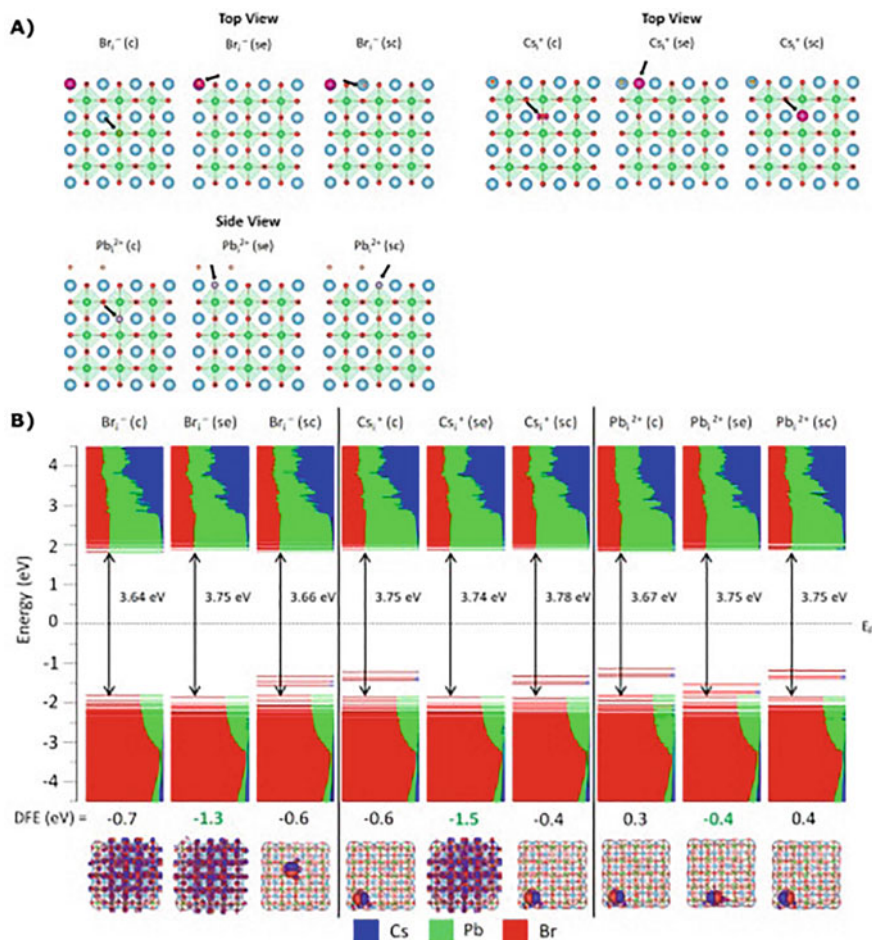


Fig. 17 **a** Illustration of the interstitial defects in the core, surface centre and surface edge of the NCs. **b** Density of states (DOS) calculated using PBE/PBE0 exchange–correlation functionals. The dotted line refers to the Fermi energy (E_F) level [120]

overall charge (Fig. 18a). From Fig. 18b, we can observe that to create these vacancies an external energy ranging from 1.4–2.3 eV is required which ultimately signifies the presence of very low vacancy densities. The creation of a neutral vacancy due to the removal of metal halide salts is energetically more favourable at the surface than in the core of the NC. However, these vacancies do not engage in the formation of any trap states irrespective of their type and position. Generally, the mid-band states originate when CsBr moieties, in large quantities, are removed from the outer surface of the NC lattice [125]. Moreover, attaining this kind of situation is very difficult due to the high DFE of these vacancies. Experimentally, the synthesized perovskite NCs are not ideal, where, the metalorganic salts for instance alkylammonium bromides

are present at the surface than the simple CsBr as considered in the calculations. The moderate solubility of the surfactants in the organic solvent leads to the loss of these capping species. This results in the stripping of the metal halide salts during the purification process and promotes the formation of a large number of surface vacancies [122]. In this case, PL efficiency reduces due to the introduction of trap states. In contrast, the formation of the antisite i.e. the exchange of a cation position with an anion finally results in the reorganization of the structure to a non-antisite configuration (back-flipping of the corresponding ions to their original position). Due to this, the shallow traps are formed which do not affect electronic properties of the NCs significantly.

PL spectroscopy helps in gaining information about the excited states and charge dynamics of a semiconducting material. The technique, thus, can be used efficiently for the complete understanding of the electro-optical properties of MHP NCs. Generally, the high efficiency in halide perovskites is related to the fast generation of electron–hole pairs as a result of photo-illumination and long diffusion lengths. In addition to this, high PLQY as shown by these materials made possible the efficient use of MHP NCs for optoelectronic applications. For high emission intensity (PL), the efficient charge recombination is needed. However, charge trapping (electron/hole) after photogeneration in the mid-band defect states often results in non-radiative recombination. More importantly, the environmental factors such as air, O₂, moisture etc. affect significantly the density of the defects in the “soft” crystal lattices of MHPs majorly due to the trapped carriers [126, 127]. The trap-mediated carrier dynamics in MHP NCs can be effectively controlled once the reasons for optical instability in these materials under various environmental conditions are well understood. In this context, it is imperative to study the PL intermittency i.e., blinking in MHP NCs under ambient conditions to understand the nature of the defects.

4.2.2 Defect-Mediated Carrier Recombination in MHP NCs Favoured by Atmospheric Constituents

Initially, LHPs grabbed much attention for their efficient use in photovoltaic devices, however, over the past few years, their use in optoelectronic applications such as LEDs or lasers has been promising [55]. It is important to note that the emissive properties of MHP crystals might change with reduction in their size. Roy et al. reported the phase transition of MAPbBr₃ NPLs from quasi-2D to 3D under photo-illumination, typically referred as photo-driven phase transformation (PDPT) process [128]. Here, the red shift (78 nm) as well as PL quenching of emission spectra was observed under continuous photo-illumination as a result of increase in the layer thickness of the perovskite platelets. This can be explained in two steps: first involves the removal of the barrier layer i.e. the surfactants (OLm) from the surface of the NPLs due to the external energy supplied to the system in the form of photon irradiation. Due to the low binding energy of the surfactants, the ligands easily get released, resulting in the formation of surface defects promoting carrier trapping. The trap states, thus formed, stimulate the non-radiative recombination leading to quenching

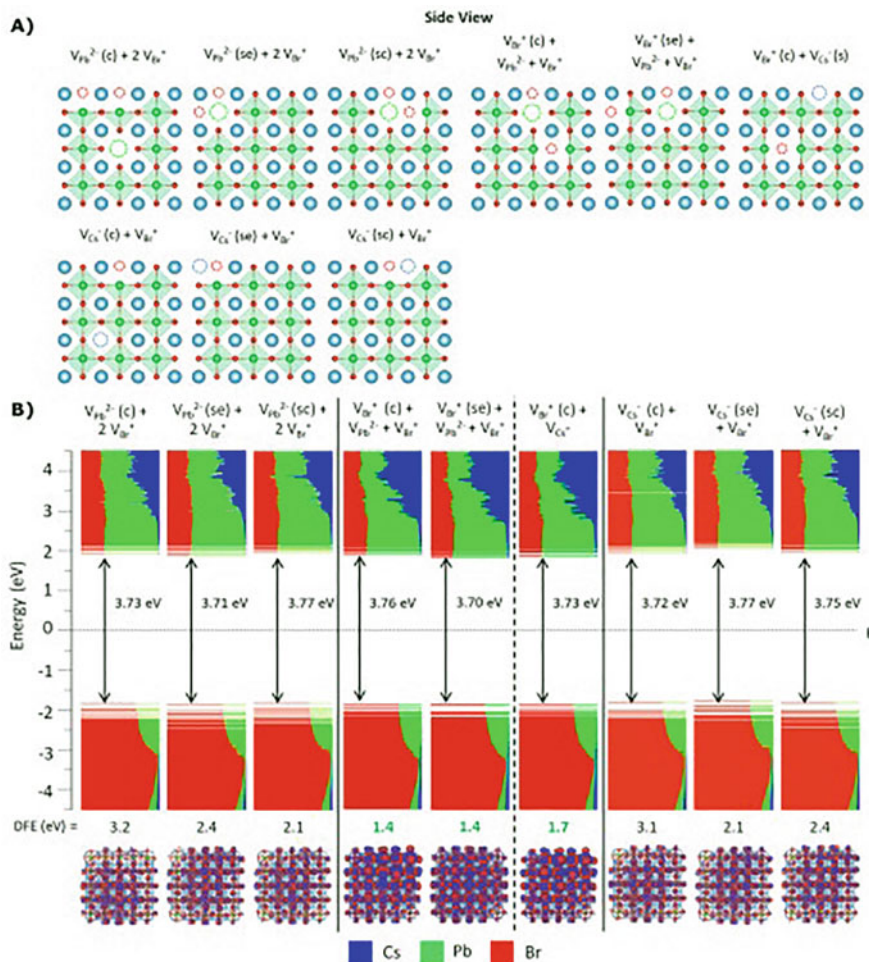


Fig. 18 **a** Illustration of the vacancy defects in the core, surface centre and surface edge of the NCs. **b** Density of states (DOS) calculated using PBE/PBE0 exchange–correlation functionals. The dotted line refers to the Fermi energy (E_F) level [120]

of the emission spectra. Second is the coalescence of the perovskite layers due to the strong ion mobilization between them to form a 3D structure. Recently, various groups also reported the observation of intermittency or blinking in PL when MHP NCs are subjected to continuous light illumination [129, 130]. In case of hybrid organic–inorganic lead-based halide perovskites, the intermittency or blinking is observed in nanostructures with size well above the Bohr’s exciton radius [131]. Mukherjee et al. studied the interaction of the organo-metallic halide perovskite (OHP) NCs with surrounding gases in order to probe the nature of the active defects present in these NCs and their influence on the carrier dynamics [132]. For this,

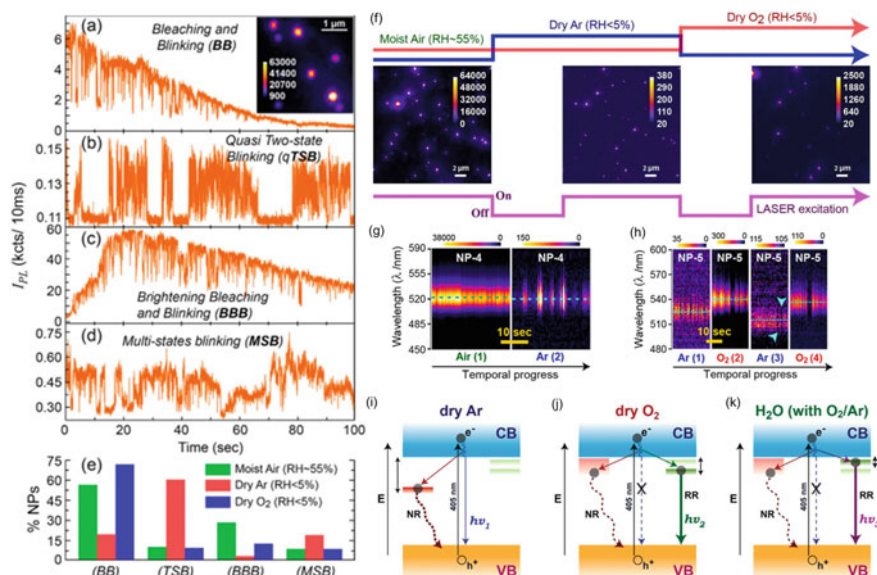


Fig. 19 a–d Different PL intermittency and intensity (I_{PL}) trajectories of various individual MAPbBr₃ NPs under similar environmental conditions. e PL blinking frequency under moist air (investigated for 221 emitters), dry Ar (investigated for 504 emitters) and dry O₂ (investigated for 604 emitters). f Inhomogeneous emission intensity of MAPbBr₃ NPs as shown by PL images under varied atmospheres. g Maximum emission intensity in ambient air decreases substantially by about 200 times in dry Ar whereas, h further tenfold increment in emission intensity was observed in dry O₂ environment. Illustration representing the pathways for charge carrier recombination under i dry Ar, j dry O₂ and k moist O₂ or Ar. The straight and dashed lines represent the radiative (RR) and non-radiative (NR) recombination, respectively. The thickness of lines represents the efficiencies qualitatively [132].

the authors first investigated the temporal instabilities of PL spectra of MAPbBr₃ NPLs under different environment conditions such as dry and humid Argon (Ar) and O₂ as well as moist (RH ~ 55%) ambient environment (Air). Figure 18a–d shows the various PL intensity (I_{PL}) trajectories of different individual NPs under similar conditions (ambient air). Based on these observations, the temporal fluctuations or blinking of single NPs can be classified into *as-stated* four categories: “(a) Bleaching with blinking (BB) (high initial intensity), (b) Quasi two-state blinking (qTSB) (low to moderate intensity) (c) Photo-brightening and bleaching with blinking (BBB) (moderate to high intensity) and (d) Multistate blinking (MSB) (low to moderate intensity)” [132]. Further, on changing the surrounding environment, the remarkable variation in the behaviour of the emitters was noticed. As evident from Fig. 16e, when the measurements were done in moist air, BB (~57%) was the dominant type of blinking among the emitters (221 individual NPs were investigated) however, in an inert atmosphere (dry Ar), there was a significant drop in the PL intensity with majority of qTSB (~60%) type blinking along with minor MSB behaviour (~20%). On the other hand, a considerable improvement in PL intensity was observed for

~75% of NPLs (out of 605 emitters) with BB type blinking in case of dry O₂ atmosphere. Furthermore, a drastic change in PL with sequential variation in atmospheric constituents i.e., moist air to dry Ar to dry O₂ (Fig. 18f) revealed maximum emission intensity in ambient air which decreased substantially (200 times; Fig. 18g) in dry Ar. Further increment in emission intensity (tenfold; Fig. 18h) was observed in dry O₂ environment. PL quenching in the presence of vacuum or inert atmosphere is mainly ascribed to the formation of deep (mid-band) defect states due to the presence of halide vacancy or interstitial sites as a result of photo-assisted halide ion migration [131]. These defect states act as non-radiative centres for long-lived charge carrier trapping, subsequently quenching the emission intensity (Fig. 18i). On the other hand, relatively deep and shallow defect states are formed in case of O₂ and moisture environment, rendering efficient radiative recombination, as seen from Fig. 18j, k. The electron coordinating oxygen in O₂/H₂O constituents help in curing the surface defects with the help of photo-generated carriers (the formation of O₂⁻ superoxides as a result of the interaction of O₂ with free electrons), thereby, passivating the non-radiative defects and result in the enhancement of emission intensity with mostly On-type intermittency [133]. However, prolonged exposure with moist O₂ under light illumination permanently degrade the material with irreversible spectral changes whereas, PL intensity could be restored while going from moist to dry conditions in inert (Ar) atmosphere. This concludes that individually O₂ or moisture does not have adverse effect on the optical properties of MHP NCs as the combination of two i.e., moist O₂ has on the spectral stability of these materials.

Tian et al. reported that the chemical/crystal defects attributing to the formation of trapping sites are often present on the surfaces (corners or edges) with large geometrical distortions exposed to the ambient conditions [129]. The defect site can act as a PL quencher or an emitter based on the chemical structure which leads to the formation of different local energy levels [134]. The PL blinking in MHP NCs might be due to the activation and deactivation of these defect states under light illumination. Additionally, as seen earlier, emission intensity gets adversely affected due to the combined effect of O₂ with moisture which increases the density of such defects into the material and further leads to an enhanced non-radiative recombination. This has a detrimental effect on the radiative efficiency and might affect the charge transport properties of the material as well. Therefore, it is very crucial to control the population of these defects in order to make efficient use of these perovskite NCs.

5 Summary

To summarize, we have presented several syntheses methods and their advantages/disadvantages for the preparation of halides perovskite nanocrystals. A deeper insight about the possible defects and their role in dictating optoelectronic properties is portrayed in detail both from theoretical as well as experimental perspective. HI method can be used successfully in the preparation of monodisperse and high-quality LHP NCs with a good control over their composition, shape (QDs, NPLs,

NRs, nanocubes and NWs), size and distribution. The use of halide salts both as a source for metal cation and halogen result in the formation of halide deficit NCs. The undercoordinated lead atoms/NPs thus formed on the surface lead to the non-radiative recombination thereby, quenching the PL emission. This encouraged the development of the modified-HI synthesis method which employs the use of benzoyl or silyl halides (halide-rich conditions) and provided the flexibility to change the metal to halide ratio for a precise composition control. However, the stripping of the metal halide salts during the purification process promotes the formation of large number of surface vacancies. Theoretically calculated defect formation energies (DFEs) for the interstitial, vacancy and antisite defects at different sites i.e., core, surface-centre and surface-edge of the NC showed the surface to be the most stable position for defect formation in NCs. Interestingly, only the excessive detachment of capping species from the surface of NCs leave behind the undercoordinated X^- (halide) ions which might lead to the formation of deep trap states. Additionally, the vacancies at the surface of NCs trap moisture or O_2 present in the environment and accelerate degradation of the perovskite NCs.

References

1. Wells HL (1893) *Z Anorg Chem* 3:195–210
2. Mitzi DB, Chondroudis K, Kagan CR (2001) *IBM J Res Dev* 45:29–45
3. Mitzi DB, Feild CA, Harrison WTA, Guloy AM (1994) *Nature* 369:467–469
4. Kojima A, Teshima K, Shirai Y, Miyasaka T (2009) *J Am Chem Soc* 131:6050–6051
5. Kim H-S, Lee C-R, Im J-H, Lee K-B, Moehl T, Marchioro A, Moon S-J, Humphry-Baker R, Yum J-H, Moser JE, Grätzel M, Park N-G (2012) *Sci Rep* 2:591
6. Chung I, Lee B, He J, Chang RPH, Kanatzidis MG (2012) *Nature* 485:486–489
7. *N T Energy J* (2020)
8. Xing G, Mathews N, Sun S, Lim Swee S, Lam Yeng M, Grätzel M, Mhaisalkar S, Sum Tze C (2013) *Science* 342:344–347
9. Manser JS, Christians JA, Kamat PV (2016) *Chem Rev* 116:12956–13008
10. Tan Z-K, Moghaddam RS, Lai ML, Docampo P, Higler R, Deschler F, Price M, Sadhanala A, Pazos LM, Credgington D, Hanusch F, Bein T, Snaith HJ, Friend RH (2014) *Nat Nanotechnol* 9:687–692
11. Deschler F, Price M, Pathak S, Klintberg LE, Jarausch D-D, Higler R, Hüttner S, Leijtens T, Stranks SD, Snaith HJ, Atatüre M, Phillips RT, Friend RH (2014) *J Phys Chem Lett* 5:1421–1426
12. D’Innocenzo V, Srimath Kandada AR, De Bastiani M, Gandini M, Petrozza A (2014) *J Am Chem Soc* 136:17730–17733
13. Zhang L, Yang X, Jiang Q, Wang P, Yin Z, Zhang X, Tan H, Yang YM, Wei M, Sutherland BR, Sargent EH, You J (2017) *Nat Commun* 8:15640
14. de Quilletes Dane W, Vorpahl Sarah M, Stranks Samuel D, Nagaoka H, Eperon Giles E, Ziffer Mark E, Snaith Henry J, Ginger David S (2015) *Science* 348:683–686
15. Uratani H, Yamashita K (2017) *J Phys Chem Lett* 8:742–746
16. Soe CMM, Nagabhushana GP, Shivaramaiah R, Tsai H, Nie W, Blancon J-C, Melkonyan F, Cao DH, Traoré B, Pedesseau L, Kepenekian M, Katan C, Even J, Marks TJ, Navrotsky A, Mohite AD, Stoumpos CC, Kanatzidis MG (2019) *Proc Natl Acad Sci* 116:58
17. Bohn BJ, Tong Y, Gramlich M, Lai ML, Döblinger M, Wang K, Hoye RLZ, Müller-Buschbaum P, Stranks SD, Urban AS, Polavarapu L, Feldmann J (2018) *Nano Lett* 18:5231–5238

18. Zheng Y, Niu T, Ran X, Qiu J, Li B, Xia Y, Chen Y, Huang W (2019) *J Mater Chem A* 7:13860–13872
19. Li C, Li J, Li Z, Zhang H, Dang Y, Kong F (2021) *CrystEngComm* 23:3619–3630
20. Schmidt LC, Pertegás A, González-Carrero S, Malinkiewicz O, Agouram S, Mínguez Espallargas G, Bolink HJ, Galian RE, Pérez-Prieto J (2014) *J Am Chem Soc* 136:850–853
21. Gonzalez-Carrero S, Galian RE, Pérez-Prieto J (2015) *J Mater Chem A* 3:9187–9193
22. Zhang F, Zhong H, Chen C, Wu X-G, Hu X, Huang H, Han J, Zou B, Dong Y (2015) *ACS Nano* 9:4533–4542
23. Imran M, Di Stasio F, Dang Z, Canale C, Khan AH, Shamsi J, Brescia R, Prato M, Manna L (2016) *Chem Mater* 28:6450–6454
24. Zhang D, Yang Y, Bekenstein Y, Yu Y, Gibson NA, Wong AB, Eaton SW, Kornienko N, Kong Q, Lai M, Alivisatos AP, Leone SR, Yang P (2016) *J Am Chem Soc* 138:7236–7239
25. Akkerman QA, Motti SG, Srimath Kandada AR, Mosconi E, D’Innocenzo V, Bertoni G, Marras S, Kamino BA, Miranda L, De Angelis F, Petrozza A, Prato M, Manna L (2016) *J Am Chem Soc* 138:1010–1016
26. Huang H, Polavarapu L, Sichert JA, Susha AS, Urban AS, Rogach AL (2016) *NPG Asia Mater* 8:e328–e328
27. Bekenstein Y, Koscher BA, Eaton SW, Yang P, Alivisatos AP (2015) *J Am Chem Soc* 137:16008–16011
28. Dutta A, Behera RK, Pal P, Baitalik S, Pradhan N (2019) *Angew Chem Int Ed* 58:5552–5556
29. Zhong Q, Cao M, Xu Y, Li P, Zhang Y, Hu H, Yang D, Xu Y, Wang L, Li Y, Zhang X, Zhang Q (2019) *Nano Lett* 19:4151–4157
30. Hintermayr VA, Richter AF, Ehrat F, Döblinger M, Vanderlinden W, Sichert JA, Tong Y, Polavarapu L, Feldmann J, Urban AS (2016) *Adv Mater* 28:9478–9485
31. Nedelcu G, Protesescu L, Yakunin S, Bodnarchuk MI, Grotevent MJ, Kovalenko MV (2015) *Nano Lett* 15:5635–5640
32. De Roo J, Ibáñez M, Geiregat P, Nedelcu G, Walravens W, Maes J, Martins JC, Van Driessche I, Kovalenko MV, Hens Z (2016) *ACS Nano* 10:2071–2081
33. Behera RK, Das Adhikari S, Dutta SK, Dutta A, Pradhan N (2018) *J Phys Chem Lett* 9:6884–6891
34. Koscher BA, Swabeck JK, Bronstein ND, Alivisatos AP (2017) *J Am Chem Soc* 139:6566–6569
35. Manspeaker C, Venkatesan S, Zakhidov A, Martirosyan KS (2017) *Curr Opin Chem Eng* 15:1–7
36. Kim S, Bae S, Lee S-W, Cho K, Lee KD, Kim H, Park S, Kwon G, Ahn S-W, Lee H-M, Kang Y, Lee H-S, Kim D (2017) *Sci Rep* 7:1200
37. Li J, Dong Q, Li N, Wang L (2017) *Adv Energy Mater* 7:1602922
38. McClure ET, Ball MR, Windl W, Woodward PM (2016) *Chem Mater* 28:1348–1354
39. Slavney AH, Hu T, Lindenberg AM, Karunadasa HI (2016) *J Am Chem Soc* 138:2138–2141
40. Volonakis G, Filip MR, Haghighirad AA, Sakai N, Wenger B, Snaith HJ, Giustino F (2016) *J Phys Chem Lett* 7:1254–1259
41. Zhang C, Gao L, Teo S, Guo Z, Xu Z, Zhao S, Ma T (2018) *Sustain Energy Fuels* 2:2419–2428
42. Volonakis G, Haghighirad AA, Milot RL, Sio WH, Filip MR, Wenger B, Johnston MB, Herz LM, Snaith HJ, Giustino F (2017) *J Phys Chem Lett* 8:772–778
43. Bhawna, Roy M, Vikram, Borkar H, Alam A, Aslam M (2021) *Chem Commun* 57:1478–1481
44. Bhawna V, Roy M, Ghorui S, Alam A, Aslam M (2022) *J Mater Chem C*. <https://doi.org/10.1039/D1TC05877K>
45. Kongsabanik J, Ghorui S, Aslam M, Alam A (2020) *Phys Rev Appl* 13:014005
46. Roy M, Ghorui S, Bhawna, Kongsabanik J, Yadav R, Alam A, Aslam M (2020) *J Phys Chem C* 124:19484–19491
47. Dey A, Ye J, De A, Debroye E, Ha SK, Bladt E, Kshirsagar AS, Wang Z, Yin J, Wang Y, Quan LN, Yan F, Gao M, Li X, Shamsi J, Debnath T, Cao M, Scheel MA, Kumar S, Steele JA, Gerhard M, Chouhan L, Xu K, Wu X-G, Li Y, Zhang Y, Dutta A, Han C, Vincon I, Rogach AL, Nag A, Samanta A, Korgel BA, Shih C-J, Gamelin DR, Son DH, Zeng H, Zhong H, Sun

- H, Demir HV, Scheblykin IG, Mora-Seró I, Stolarczyk JK, Zhang JZ, Feldmann J, Hofkens J, Luther JM, Pérez-Prieto J, Li L, Manna L, Bodnarchuk MI, Kovalenko MV, Roeffaers MBJ, Pradhan N, Mohammed OF, Bakr OM, Yang P, Müller-Buschbaum P, Kamat PV, Bao Q, Zhang Q, Krahn R, Galian RE, Stranks SD, Bals S, Biju V, Tisdale WA, Yan Y, Hoye RLZ, Polavarapu L (2021) *ACS Nano* 15:10775–10981
48. Zheng X, Hou Y, Sun H-T, Mohammed OF, Sargent EH, Bakr OM (2019) *J Phys Chem Lett* 10:2629–2640
 49. Stranks SD, Burlakov VM, Leijtens T, Ball JM, Goriely A, Snaith HJ (2014) *Phys Rev Appl* 2:034007
 50. Srimath Kandada AR, Neutzner S, D’Innocenzo V, Tassone F, Gandini M, Akkerman QA, Prato M, Manna L, Petrozza A, Lanzani G (2016) *J Am Chem Soc* 138:13604–13611
 51. Rossetti R, Nakahara S, Brus LE (1983) *J Chem Phys* 79:1086–1088
 52. Brus L (1986) *J Phys Chem* 90:2555–2560
 53. Li X, Cao F, Yu D, Chen J, Sun Z, Shen Y, Zhu Y, Wang L, Wei Y, Wu Y, Zeng H (2017) *Small* 13:1603996
 54. Yang D, Cao M, Zhong Q, Li P, Zhang X, Zhang Q (2019) *J Mater Chem C* 7:757–789
 55. Veldhuis SA, Boix PP, Yantara N, Li M, Sum TC, Mathews N, Mhaisalkar SG (2016) *Adv Mater* 28:6804–6834
 56. Protesescu L, Yakunin S, Bodnarchuk MI, Krieg F, Caputo R, Hendon CH, Yang RX, Walsh A, Kovalenko MV (2015) *Nano Lett* 15:3692–3696
 57. Giustino F, Snaith HJ (2016) *ACS Energy Lett* 1:1233–1240
 58. Cortecchia D, Dewi HA, Yin J, Bruno A, Chen S, Baikie T, Boix PP, Grätzel M, Mhaisalkar S, Soci C, Mathews N (2016) *Inorg Chem* 55:1044–1052
 59. Pilania G, Balachandran PV, Kim C, Lookman T (2016) *Front Mater* 3:19
 60. Correa-Baena J-P, Saliba M, Buonassisi T, Grätzel M, Abate A, Tress W, Hagfeldt A (2017) *Science* 358:739–744
 61. Protesescu L, Yakunin S, Kumar S, Bär J, Bertolotti F, Masciocchi N, Guagliardi A, Grotevent M, Shorubalko I, Bodnarchuk MI, Shih CJ, Kovalenko MV (2017) *ACS Nano* 11:3119–3134
 62. Snaith HJ (2018) *Nat Mater* 17:372–376
 63. Kim G-W, Petrozza A (2020) *Adv Energy Mater* 10:2001959
 64. Zakutayev A, Caskey CM, Fioretti AN, Ginley DS, Vidal J, Stevanovic V, Tea E, Lany S (2014) *J Phys Chem Lett* 5:1117–1125
 65. Brandt RE, Poindexter JR, Gorai P, Kurchin RC, Hoye RLZ, Nienhaus L, Wilson MWB, Polizzotti JA, Sereika R, Žaltauskas R, Lee LC, MacManus-Driscoll JL, Bawendi M, Stevanović V, Buonassisi T (2017) *Chem Mater* 29:4667–4674
 66. Protesescu L, Yakunin S, Nazarenko O, Dirin DN, Kovalenko MV (2018) *ACS Appl Nano Mater* 1:1300–1308
 67. Murray CB, Norris DJ, Bawendi MG (1993) *J Am Chem Soc* 115:8706–8715
 68. Bullen CR, Mulvaney P (2004) *Nano Lett* 4:2303–2307
 69. Roy M, Vikram, Banerjee S, Mitra A, Alam A, Aslam M (2019) *Chem—A European J* 25:9892–9901
 70. Pan A, He B, Fan X, Liu Z, Urban JJ, Alivisatos AP, He L, Liu Y (2016) *ACS Nano* 10:7943–7954
 71. Vybornyi O, Yakunin S, Kovalenko MV (2016) *Nanoscale* 8:6278–6283
 72. Protesescu L, Yakunin S, Bodnarchuk MI, Bertolotti F, Masciocchi N, Guagliardi A, Kovalenko MV (2016) *J Am Chem Soc* 138:14202–14205
 73. Lignos I, Protesescu L, Emiroglu DB, Maceiczky R, Schneider S, Kovalenko MV, deMello AJ (2018) *Nano Lett* 18:1246–1252
 74. Protesescu L, Yakunin S, Kumar S, Bär J, Bertolotti F, Masciocchi N, Guagliardi A, Grotevent M, Shorubalko I, Bodnarchuk MI, Shih C-J, Kovalenko MV (2017) *ACS Nano* 11:3119–3134
 75. Akkerman QA, Park S, Radicchi E, Nunzi F, Mosconi E, De Angelis F, Brescia R, Rastogi P, Prato M, Manna L (2017) *Nano Lett* 17:1924–1930
 76. Han C, Li C, Zang Z, Wang M, Sun K, Tang X, Du J (2017) *Photon Res* 5:473–480

77. Yuan L, Patterson R, Wen X, Zhang Z, Conibeer G, Huang S (2017) *J Colloid Interface Sci* 504:586–592
78. Woo JY, Kim Y, Bae J, Kim TG, Kim JW, Lee DC, Jeong S (2017) *Chem Mater* 29:7088–7092
79. Liu P, Chen W, Wang W, Xu B, Wu D, Hao J, Cao W, Fang F, Li Y, Zeng Y, Pan R, Chen S, Cao W, Sun XW, Wang K (2017) *Chem Mater* 29:5168–5173
80. Yassitepe E, Yang Z, Voznyy O, Kim Y, Walters G, Castañeda JA, Kanjanaboos P, Yuan M, Gong X, Fan F, Pan J, Hoogland S, Comin R, Bakr OM, Padilha LA, Nogueira AF, Sargent EH (2016) *Adv Func Mater* 26:8757–8763
81. Imran M, Caligiuri V, Wang M, Goldoni L, Prato M, Krahn R, De Trizio L, Manna L (2018) *J Am Chem Soc* 140:2656–2664
82. Creutz SE, Crites EN, De Siena MC, Gamelin DR (2018) *Nano Lett* 18:1118–1123
83. Yuan Z, Shu Y, Xin Y, Ma B (2016) *Chem Commun* 52:3887–3890
84. Zhang D, Eaton SW, Yu Y, Dou L, Yang P (2015) *J Am Chem Soc* 137:9230–9233
85. Shamsi J, Urban AS, Imran M, De Trizio L, Manna L (2019) *Chem Rev* 119:3296–3348
86. Almeida G, Goldoni L, Akkerman Q, Dang Z, Khan AH, Marras S, Moreels I, Manna L (2018) *ACS Nano* 12:1704–1711
87. Zhang D, Yu Y, Bekenstein Y, Wong AB, Alivisatos AP, Yang P (2016) *J Am Chem Soc* 138:13155–13158
88. Chen M, Zou Y, Wu L, Pan Q, Yang D, Hu H, Tan Y, Zhong Q, Xu Y, Liu H, Sun B, Zhang Q (2017) *Adv Func Mater* 27:1701121
89. Li X, Wu Y, Zhang S, Cai B, Gu Y, Song J, Zeng H (2016) *Adv Func Mater* 26:2435–2445
90. Pan Q, Hu H, Zou Y, Chen M, Wu L, Yang D, Yuan X, Fan J, Sun B, Zhang Q (2017) *J Mater Chem C* 5:10947–10954
91. Tong Y, Bladt E, Aygüler MF, Manzi A, Milowska KZ, Hintermayr VA, Docampo P, Bals S, Urban AS, Polavarapu L, Feldmann J (2016) *Angew Chem Int Ed* 55:13887–13892
92. Wei S, Yang Y, Kang X, Wang L, Huang L, Pan D (2016) *Chem Commun* 52:7265–7268
93. Shamsi J, Rastogi P, Caligiuri V, Abdelhady AL, Spirito D, Manna L, Krahn R (2017) *ACS Nano* 11:10206–10213
94. Papavassiliou GC, Pagona G, Karousis N, Mousdis GA, Koutselas I, Vassilakopoulou A (2012) *J Mater Chem* 22:8271–8280
95. Hung H, Susha AS, Kershaw SV, Hung TF, Rogach AL (2015) *Adv Sci* 2:1500194
96. Zhao Y, Xu X, You X (2016) *Sci Rep* 6:35931
97. Shamsi J, Abdelhady AL, Accornero S, Arciniegas M, Goldoni L, Kandada ARS, Petrozza A, Manna L (2016) *ACS Energy Lett* 1:1042–1048
98. Levchuk I, Osvet A, Tang X, Brandl M, Perea JD, Hoegl F, Matt GJ, Hock R, Batentschuk M, Brabec CJ (2017) *Nano Lett* 17:2765–2770
99. Seth S, Samanta A (2016) *Sci Rep* 6:37693
100. Ahmed GH, Yin J, Bose R, Sinatra L, Alarousu E, Yengel E, AlYami NM, Saidaminov MI, Zhang Y, Hedhili MN, Bakr OM, Brédas J-L, Mohammed OF (2017) *Chem Mater* 29:4393–4400
101. Sichert JA, Tong Y, Mutz N, Vollmer M, Fischer S, Milowska KZ, García Cortadella R, Nickel B, Cardenas-Daw C, Stolarczyk JK, Urban AS, Feldmann J (2015) *Nano Lett* 15:6521–6527
102. Kumar S, Jagielski J, Yakunin S, Rice P, Chiu Y-C, Wang M, Nedelcu G, Kim Y, Lin S, Santos EJG, Kovalenko MV, Shih C-J (2016) *ACS Nano* 10:9720–9729
103. Kirakosyan A, Kim J, Lee SW, Swathi I, Yoon S-G, Choi J (2017) *Cryst Growth Des* 17:794–799
104. Levchuk I, Herre P, Brandl M, Osvet A, Hock R, Peukert W, Schweizer P, Spiecker E, Batentschuk M, Brabec CJ (2017) *Chem Commun* 53:244–247
105. Zhang F, Huang S, Wang P, Chen X, Zhao S, Dong Y, Zhong H (2017) *Chem Mater* 29:3793–3799
106. Li X, Yu D, Cao F, Gu Y, Wei Y, Wu Y, Song J, Zeng H (2016) *Adv Func Mater* 26:5903–5912
107. Roy M, Vikram B, Dedhia U, Alam A, Aslam M (2021) *J Phys Chem Lett* 12:1189–1194
108. Parveen S, Paul KK, Giri PK (2020) *ACS Appl Mater Interfaces* 12:6283–6297
109. Jang DM, Kim DH, Park K, Park J, Lee JW, Song JK (2016) *J Mater Chem C* 4:10625–10629

110. Leupold N, Schötz K, Cacovich S, Bauer I, Schultz M, Daubinger M, Kaiser L, Rebai A, Rousset J, Köhler A, Schulz P, Moos R, Panzer F (2019) *ACS Appl Mater Interfaces* 11:30259–30268
111. Zhu Z-Y, Yang Q-Q, Gao L-F, Zhang L, Shi A-Y, Sun C-L, Wang Q, Zhang H-L (2017) *J Phys Chem Lett* 8:1610–1614
112. Baláz P, Achimovičová M, Baláz M, Billik P, Cherkezova-Zheleva Z, Criado JM, Delogu F, Dutková E, Gaffet E, Gotor FJ, Kumar R, Mitov I, Rojac T, Senna M, Streletskii A, Wieczorek-Ciurowa K (2013) *Chem Soc Rev* 42:7571–7637
113. McCluskey MD, Janotti A (2020) *J Appl Phys* 127:190401
114. Queisser Hans J, Haller Eugene E (1998) *Science* 281:945–950
115. Shockley W, Read WT (1952) *Phys Rev* 87:835–842
116. Tress W (2016). https://doi.org/10.1007/978-3-319-35114-8_3
117. Shi W, Zhang X, Matras-Postolek K, Yang P (2021) *ACS Appl Nano Mater* 4:9391–9400
118. Paul S, Ahmed T, Das S, Samanta A (2021) *J Phys Chem C* 125:23539–23547
119. Adinolfi V, Yuan M, Comin R, Thibau ES, Shi D, Saidaminov MI, Kanjanaboos P, Kopilovic D, Hoogland S, Lu Z-H, Bakr OM, Sargent EH (2016) *Adv Mater* 28:3406–3410
120. ten Brinck S, Zaccaria F, Infante I (2019) *ACS Energy Lett* 4:2739–2747
121. Jin H, Debroye E, Keshavarz M, Scheblykin IG, Roeffaers MBJ, Hofkens J, Steele JA (2020) *Mater Horiz* 7:397–410
122. Krieg F, Ochsenhein ST, Yakunin S, ten Brinck S, Aellen P, Süess A, Clerc B, Guggisberg D, Nazarenko O, Shynkarenko Y, Kumar S, Shih C-J, Infante I, Kovalenko MV (2018) *ACS Energy Lett* 3:641–646
123. Freysoldt C, Neugebauer J, Van de Walle CG (2009) *Phys Rev Lett* 102:016402
124. Meggiolaro D, Mosconi E, De Angelis F (2018) *ACS Energy Lett* 3:447–451
125. Bodnarchuk MI, Boehme SC, ten Brinck S, Bernasconi C, Shynkarenko Y, Krieg F, Widmer R, Aeschlimann B, Günther D, Kovalenko MV, Infante I (2019) *ACS Energy Lett* 4:63–74
126. Chouhan L, Ghimire S, Biju V (2019) *Angew Chem* 131:4796–4796
127. Yang J, Yuan Z, Liu X, Braun S, Li Y, Tang J, Gao F, Duan C, Fahlman M, Bao Q (2018) *ACS Appl Mater Interfaces* 10:16225–16230
128. Roy M, Vikram B, Alam A, Aslam M (2021) *Phys Chem Chem Phys* 23:27355–27364
129. Tian Y, Merdasa A, Peter M, Abdellah M, Zheng K, Ponseca CS, Pullerits T, Yartsev A, Sundström V, Scheblykin IG (2015) *Nano Lett* 15:1603–1608
130. Yuan H, Debroye E, Caliendo G, Janssen KPF, van Loon J, Kirschhock CEA, Martens JA, Hofkens J, Roeffaers MBJ (2016) *ACS Omega* 1:148–159
131. Galisteo-López JF, Calvo ME, Rojas TC, Míguez H (2019) *ACS Appl Mater Interfaces* 11:6344–6349
132. Mukherjee A, Roy M, Pathoor N, Aslam M, Chowdhury A (2021) *J Phys Chem C* 125:17133–17143
133. Feng X, Su H, Wu Y, Wu H, Xie J, Liu X, Fan J, Dai J, He Z (2017) *J Mater Chem A* 5:12048–12053
134. Tian Y, Merdasa A, Unger E, Abdellah M, Zheng K, McKibbin S, Mikkelsen A, Pullerits T, Yartsev A, Sundström V, Scheblykin IG (2015) *J Phys Chem Lett* 6:4171–4177